Computer-Aided Design 161 (2023) 103542

Contents lists available at ScienceDirect

Computer-Aided Design

journal homepage: www.elsevier.com/locate/cad

Topology Optimization of Self-supporting Porous Structures Based on Triply Periodic Minimal Surfaces

Nan Zheng, Xiaoya Zhai *, Falai Chen

School of Mathematical Sciences, University of Science and Technology of China, Hefei, Anhui, 230026, PR China

ARTICLE INFO

Article history:
Received 29 December 2022
Received in revised form 3 April 2023
Accepted 24 April 2023

Keywords:
Topology optimization
Additive manufacturing
Self-supporting structure
Triply periodic minimal surfaces

ABSTRACT

With the advent of additive manufacturing (AM), topology optimization (TO) has become increasingly important in structural design. A key component of structural design is generating the interior shape of an object under predefined force conditions and specific constraints. Fabricating such models by layer-based AM suffers from the problem of adding and removing interior supporting structures, which can produce artifacts in the final product. In this paper, we propose an algorithm to design a self-supporting porous structure by integrating overhang constraints into the topology optimization framework. A minimum thickness constraint is also built into the optimization process to automatically enforce printability of the resulting structures. We utilize triply periodic minimal surfaces (TPMSs) to represent interior structures which can be analyzed, optimized and stored directly using analytical functions. We apply several acceleration methods including super element strategy, multigrid algorithm and GPU-based solver to handle models comprising of several million of elements efficiently. Numerical results indicate that the optimized interior structures obtained by our approach exhibit improved printability as they largely satisfy manufacturing requirements on overhang angles and minimal thicknesses.

1. Introduction

Topological optimization is a mathematical method that optimizes the interior material distribution of a 3D model to meet specific demands on its physical properties, such as resistance to external loads. It has broad applications in high-tech industries, such as aerospace [1], automotive [2], architecture [3] and bio-engineering [4]. However, the manufacture of topologically optimized structures by using traditional techniques such as Computer Numerical Control (CNC) is challenging due to the complex geometry of the optimized structures. In the past decade, additive manufacturing (3D printing) has emerged as a revolutionary manufacturing technology that enables the convenient fabrication of complex structures. Thus there is a significant interest in integrating topological optimization and additive manufacturing to design and fabricate various optimized structures.

In this paper, we focus on the design and fabrication of porous structures with additive manufacturing [5]. Porous structures offer some desirable properties such as small weight-to-stiffness ratio [6], good buffering protection [7], and excellent thermal conductivity [8]. They are widely used in various fields such as modeling human bones and dentures in medical engineering, fibrous materials in civil engineering, metal foam, insulating materials, sound-absorbing coatings and heat dissipation materials in material engineering. Triply periodic minimal surfaces (TPMSs [9]) are often utilized as a foundational element in constructing porous structures, as they are mathematically defined as minimal surfaces. They are widely used in structural optimization due to their full connections, high smoothness, non-self-intersections and quasi-self-supporting properties [10].

Previous investigations of TPMSs have mainly focused on structure optimization for lightweight [10] or mechanical properties [11,12]. However, in many cases, the optimized structures cannot be directly printed by laser-based additive manufacturing techniques such as Stereolithography Apparatus (SLA) and Fused Deposition Modeling (FDM) due to overhang regions. Additional supporting material must be added to support these regions during the printing process. After the model is printed, then the supporting material should be removed. This process causes a waste of materials and produces artifacts on the surface of the printed model. A meticulous post-processing operation is crucial to refine the surface of the printed model. Additionally, the minimum thickness of the structure is a crucial consideration. If the structure is too thin, the printer may not be able to print it correctly, leading to a significant impact on the quality of the printed model.

The goal of this paper is to utilize topology optimization to design a self-supporting porous structure based on TPMS while ensuring its stiffness. A structure is considered to be self-supported

* Corresponding author.
E-mail addresses: zhengn@mail.ustc.edu.cn (N. Zheng), xiaoya93@mail.ustc.edu.cn (X. Zhai), chenfl@ustc.edu.cn (F. Chen).

https://doi.org/10.1016/j.cad.2023.103542
0010-4485/© 2023 Elsevier Ltd. All rights reserved.

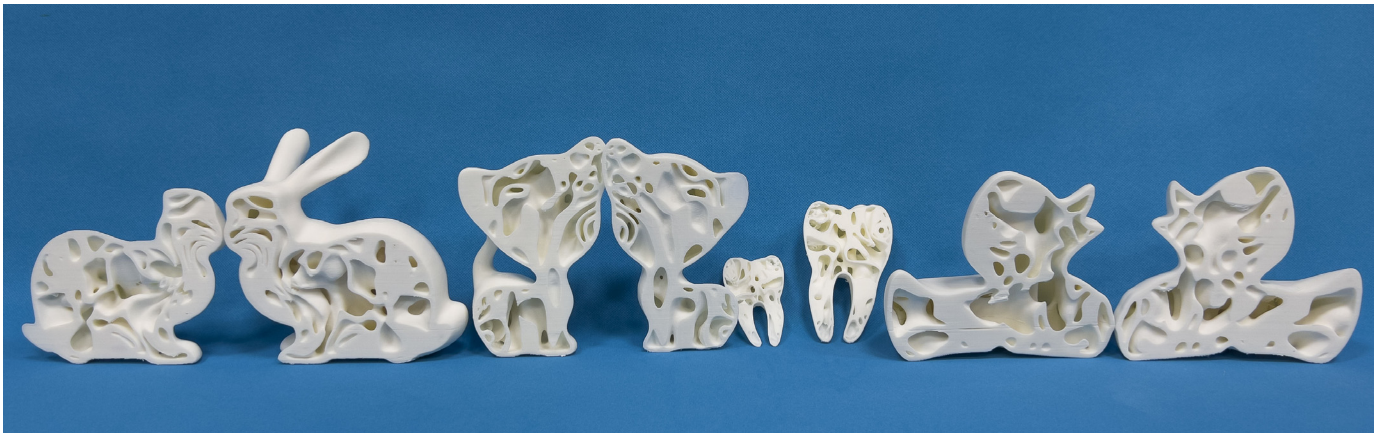

Fig. 1. 3D printing results of four models by our method.

if every point on the surface of the structure has an overhang angle smaller than a prescribed threshold [13]. To achieve this, we use TPMS-based geometry to provide an explicit expression for the normal of the boundary surface, and we build a novel global inequality constraint that guarantees self-supporting structures. We also use a weighting scheme to prevent isolated non-self-supporting points from contributing to a global constraint. Furthermore, we discretize the TPMS parameters to obtain design variables, resulting in smooth optimized designs without sharp features. A minimal thickness constraint is also imposed by restricting the design variables in some suitable intervals to ensure the printability of the models. By minimizing the compliance of the structure with the above constraints through a two-stage optimization strategy, our method generates printable and mechanically optimized porous structures effectively. We reduce the number of design variables through collocation points, which further increases the efficiency of our approach. Fig. 1 illustrates some 3D printing models generated by our algorithm.

In summary, the specific contributions of the current paper are as follows:

- A topology optimization framework is developed to generate smooth porous structures with a high self-supporting ratio based on TPMS. We formulated a new global constraint while a weighting scheme is utilized to filter out small areas that can be printed.
- Establish the relationship between minimum length constraints and the shell thickness of TPMS to ensure the printability of porous structures.
- Apply several acceleration methods, including super element strategy, multigrid algorithm, and GPU-based implementation, have been applied to efficiently solve the topology optimization problem.

2. Related work

2.1. Topology optimization

Topology optimization (TO) is an algorithmic process that optimizes the material distribution in the design domain according to the predefined boundary conditions and constraints. Many methods have been developed to solve the TO problem, such as the homogenization method [14], solid isotropic material with penalization (SIMP) [15], level set method [16], topology derivative method [17], and moving morphable components (MMC) [18]. Among them, the SIMP method is a very simple and popular method that will be adopted in the current work.

2.2. TPMS-based structure optimization

TPMSs have been taken as an efficient representation of porous structures. Due to the implicit representations of TPMSs, the properties of porous structures such as porosity and volume fraction can be easily achieved by setting suitable parameters of TPMSs [19,20]. Complex operations such as boolean, modulation, and convolutions can be applied to TPMSs [21,22].

In order to mimic natural porous structures and fulfill the demands of diverse applications, graded TPMS [23,24], heterogeneous TPMS [25,26], multi-scale TPMS [10,27] were designed. In addition, TPMSs have been widely used in the design of articular scaffolds due to their large surface areas and fully connected structures [23,28].

In recent years, TPMSs have gradually attracted the attention from the community of computer graphics and computer-aided design. Zhu et al. [29] designed a novel TPMS-based porous scaffold with optimized thickness to tune both the mechanical and biological properties. VISWANATH et al. [30] applied 3D convolutional neural network (CNN) models for the topology optimization of a unit cell based on TPMS. Li et al. [31] proposed an optimization strategy for designing models of gyroid-based functionally graded cellular structures. Hu et al. [10] constructed a multi-scale porous structure by adding parameters to control the period and volume of the TPMSs. Later they proposed an efficient TPMS-based structural optimization method [32] without remeshing operation in finite element computation. Wang et al. [33] adopted the optimization framework for the problem of steady-state heat conduction. However, these works do not take manufacturing constraints into consideration, and the resulting porous structures are hard to manufacture without additional supporting material.

2.3. Fabrication requirements

Structures generated by topology optimization are typically complex in geometry, with large overhang regions and small branches. To fabricate these structures using additive manufacturing, additional overhang constraints and minimal length constraints should be added. However, adding supporting material leads to material waste, longer fabrication time, and lower surface quality. Therefore, minimizing overhang regions and detecting and removing small branches has become an area of interest.

Many efforts have been proposed to reduce additional support materials in additive manufacturing, including optimizing the direction of fabrication [34,35] and modifying the geometries of the structures [36,37]. Paul and Anand [38] proposed a strategy to find an optimal printing direction that minimizes the volume of support structures. Qian [39] introduced constraints on the boundary shape, such as undercut control and minimal overhang angle control, that are helpful in reducing the need for support structures. Wang and Qian [40] proposed a method that optimizes both the build orientation and density field to satisfy overhang angle constraints for self-supporting parts. Allaire et al. [41] presented a new mechanical constraint functional that mimics the layer-by-layer construction process used in additive manufacturing technologies. Wu et al. [13] proposed a method to generate infill structures that satisfy manufacturing requirements on overhang-angle and wall-thickness, but is limited to rhombic cells. Mizendehdel and Suresh [37] proposed a method for reducing support structures in additive manufacturing through level set topology optimization. Garaigordobil et al. [42] introduced an overhang constraint for controlling support material in the manufacturing of compliant mechanisms. Xu et al. [43] proposed a support-free infill structure without optimization. Choi et al. [44] introduced a novel method for support-free hollowing. Yan et al. [45] utilized TPMS to define channels that adequately distribute injected materials in the shape interior. They stretched the optimized model vertically in a post-processing step to obtain self-supporting structures. Different from the previous approach, our method includes self-supporting constraints within the topology optimization framework to generate strong connected and porous objects based on an efficient TPMS-based representation.

For the minimum thickness problem, Poulsen [46] proposed to deal with it by imposing a minimum length scale constraint in topology optimization. Later Guest et al. [47] and Zhou et al. [48] presented a filtering-threshold topology optimization scheme to improve computational efficiency. In our paper, we establish associations between TPMS-based geometries and external overhang constraints and minimal length constraints to achieve better printing performance.

3. Geometric representations of porous structures

3.1. Representations of TPMS

TPMSs are minimal surfaces that have a crystalline structure and are triply periodic in the sense that they repeat themselves in three independent directions. TPMSs have two main representations—Enneper-Weierstrass parametric representation and Fourier series representation.

According to the Enneper-Weierstrass parametric representation, TPMSs can be expressed analytically as [49,50]:

$$\begin{cases} x = \mathbf{Re}\left(e^{i\theta}\int_{\omega_0}^{\omega}\left(1-\tau^2\right)R(\tau)\mathbf{d}\tau\right); \\ y = \mathbf{Re}\left(e^{i\theta}\int_{\omega_0}^{\omega}i\left(1+\tau^2\right)R(\tau)\mathbf{d}\tau\right); \\ z = \mathbf{Re}\left(e^{i\theta}\int_{\omega_0}^{\omega}2\tau R(\tau)\mathbf{d}\tau\right); \end{cases} \tag{1}$$

where i is the imaginary unit, and $R(\tau)$ is a complex function. Thus, the Cartesian coordinates of any point on a minimal surface are expressed as the real parts (**Re**) of some complex (curvilinear) integrals, evaluated in the complex plane from a fixed point ω_0 to a variable point ω. The Weierstrass function $R(\tau)$ completely specifies the local differential geometry of the surface and guarantees that the described surface is a minimal surface.

However, only a few kinds of TPMSs can be generated from the parametric function (1). An alternative mathematical representation for TPMSs can be approximated by the periodic nodal surface defined in terms of Fourier series [19]:

$$\varphi(\mathbf{r}) = \sum_{k=1}^{K} A_k \cos\left[\frac{2\pi(\mathbf{h}_k\cdot\mathbf{r})}{\lambda_k} + P_k\right] = C, \tag{2}$$

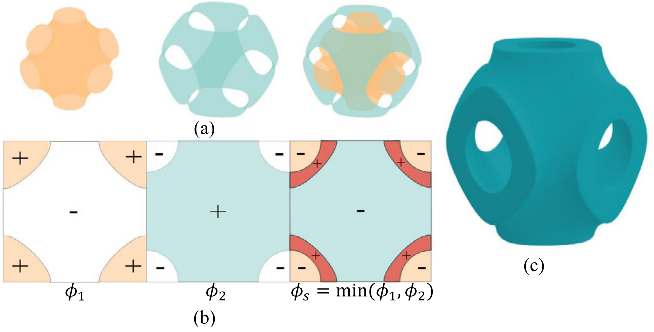

Fig. 2. Illustration of the geometry representation of a porous structure. (a) A P surface with $t_x = t_y = t_z = 1, C = 0.427$; (b) Corresponding signed distance fields on 2D plane (from left to right: ϕ_1, ϕ_2 and ϕ_s; (c) Corresponding TPMS-based porous structure.

in which $\mathbf{r} = (x, y, z) \in \mathbb{R}^3$ is a location vector, A_k is the amplitude, $\mathbf{h}_k$ is the kth reciprocal lattice vectors, λ_k is the period factor, P_k is the function phase and C is a constant. Earlier methods [51] reported that the topology of TPMSs is satisfactorily reproduced by truncating the series to the leading term, giving the following nodal approximations of P, G and D surfaces:

$$\begin{aligned} \varphi_P(\mathbf{r}) =& \cos(2\pi t_x x) + \cos(2\pi t_y y) + \cos(2\pi t_z z) = C, \\ \varphi_G(\mathbf{r}) =& \sin(2\pi t_x x)\cos(2\pi t_y y) + \sin(2\pi t_z z)\cos(2\pi t_x x) \\ &+ \sin(2\pi t_y y)\cos(2\pi t_z z) = C, \\ \varphi_D(\mathbf{r}) =& \cos(2\pi t_x x)\cos(2\pi t_y y)\cos(2\pi t_z z) \\ &- \sin(2\pi t_x x)\sin(2\pi t_y y)\sin(2\pi t_z z) = C, \end{aligned} \tag{3}$$

where t_x, t_y and t_z represent periodic parameters along x-axis, y-axis and z-axis, respectively, and C is a nonzero constant.

3.2. TPMS-based porous structures

Signed distance fields are effective representations of porous structures. In this paper, we assume that positive and negative distances determine the inside and outside of a structure, respectively. A TPMS-based porous structure can be described by the intersection of two solids that are defined by two signed distance fields:

$$\begin{aligned} &\phi_1 = \varphi + C, \\ &\phi_2 = C - \varphi, \\ &\phi_s = \min(\phi_1, \phi_2), \end{aligned} \tag{4}$$

where ϕ_1 and ϕ_2 represent two signed distance fields determined by the TPMS function φ, and C is the physical offset which measures the algebraic distance of two surfaces $\phi_i = 0$ ($i = 1$ or 2) and $\phi = 0$. The porous structure is defined by $\phi_s > 0$ which is the intersection of two solids $\phi_1 > 0$ and $\phi_2 > 0$. In order to calculate the derivatives of $\phi_s(\mathbf{r})$ at any point $\mathbf{r}$, we introduce a smooth approximation of $\phi_s(\mathbf{r})$ by:

$$\begin{aligned} \phi_s(\mathbf{r}) &= \phi_1(\mathbf{r}) + \phi_2(\mathbf{r}) - \sqrt{\phi_1^2(\mathbf{r}) + \phi_2^2(\mathbf{r})}, \\ &= 2C - \sqrt{2C^2 + 2\varphi^2}. \end{aligned} \tag{5}$$

An example is illustrated in Fig. 2, where φ is the P surface with $t_x = t_y = t_z = 1$ and $C = 0.427$. Fig. 3 show two sequences of porous structures for different parameter values of t_x, t_y, t_z and C. Variations of porosity in one unit can be clearly observed.

In our work, a TPMS-based porous structure is optimized inside a given model Ω_{Model}:

$$\phi_{opt} = \min(\phi_s, \phi_{Model}), \tag{6}$$

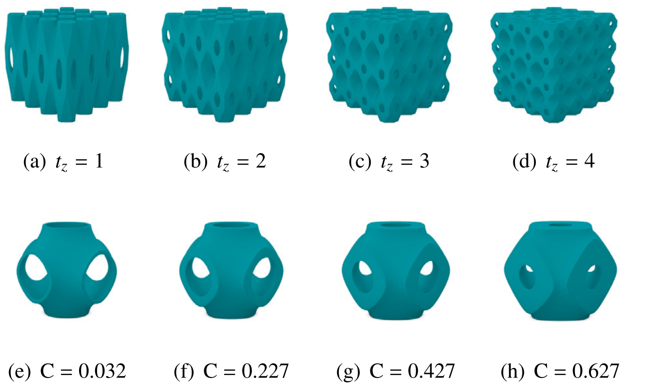

(a) $t_z = 1$ (b) $t_z = 2$ (c) $t_z = 3$ (d) $t_z = 4$

(e) C = 0.032 (f) C = 0.227 (g) C = 0.427 (h) C = 0.627

Fig. 3. TPMS-based porous structures. (a) – (d) show the structures with different period parameters along z-axis with $t_x = t_y = 4$ and $C = 0.427$. (e) – (h) show the structures with different thickness parameters with $t_x = t_y = t_z = 1$.

where ϕ_{Model} is the signed distance field of the shape Ω_{Model}. The final porous structure that fills in the interior of Ω_{Model} can be presented as $\phi_{opt} > 0$.

3.3. Design variable distribution function

In the minimal surface representations (3), $t_x(\mathbf{r})$, $t_y(\mathbf{r})$, $t_z(\mathbf{r})$ and $C(\mathbf{r})$ are free parameters that depend on the location vector $\mathbf{r}$ and determine the shapes of the minimal surfaces. They are the design variables of our TO problem. In order to efficiently represent and compute these variables, we interpolate them using radial basis functions at a set of collocation points $\{\mathbf{r}_i\}_{i=1}^n$ that are uniformly arranged in space [52]:

$$t_x(\mathbf{r}) = \sum_{k=1}^{n} \alpha_k f(\|\mathbf{r} - \mathbf{r}_k\|_2) + \sum_{l=1}^{q} \beta_l p_l(\mathbf{r}), \tag{7}$$

where $f(x) = x^2 \log(x)$ is the polyharmonic radial basis function, n is the number of the collocation points, q is the number of polynomial basis functions, $p_l(\mathbf{r})$, $l = 1, \dots, q$ are polynomial basis functions.

There are q additional degrees of freedom in (7), and they are fixed by q additional homogeneous equations. This augmented system has a unique solution:

$$\begin{aligned} \sum_{k=1}^{n} \alpha_k f(\|\mathbf{r}_i - \mathbf{r}_k\|_2) + \sum_{l=1}^{q} \beta_l p_l(\mathbf{r}_i) &= t_x(\mathbf{r}_i), \ 1 \le i \le n; \\ \sum_{k=1}^{n} \alpha_k p_l(\mathbf{r}_k) = 0, \qquad & 1 \le l \le q; \end{aligned} \tag{8}$$

where $t_x(\mathbf{r}_i)$ is the x-axis period variable at the ith collocation point. We solve the linear system of Eqs. (8) by the known $\{t_x(\mathbf{r}_i)\}_{i=1}^n$ in the previous iteration to compute the unknown coefficient $\{\alpha_k\}_{k=1}^n$ and $\{\beta_l\}_{l=1}^q$. Thus the expression for $t_x(\mathbf{r})$ is obtained. The variable distribution functions of $t_y(\mathbf{r})$, $t_z(\mathbf{r})$ and $C(\mathbf{r})$ can be computed in a similar way.

4. Methods

4.1. Problem and formulation

Problem. The goal of the current work is to find an interior material distribution ϕ_{opt} with self-supporting requirement and maximum stiffness under predefined volume fraction in a given design domain ϕ_M.

Formulation. This problem can be formulated as the following optimization problem:

$$(\mathcal{P}): \quad \min_{t_x(\mathbf{r}), t_y(\mathbf{r}), t_z(\mathbf{r}), C(\mathbf{r})} \quad \mathbf{I} = \mathbf{U}^{\mathrm{T}}\mathbf{F}, \tag{9}$$

$$\text{s.t.} \quad V(t_x(\mathbf{r}), t_y(\mathbf{r}), t_z(\mathbf{r}), C(\mathbf{r})) \le V_0, \tag{10}$$

$$\alpha \le \alpha_0, \tag{11}$$

$$\mathbf{KU} = \mathbf{F}, \tag{12}$$

$$t_{min} \le t_x(\mathbf{r}), t_y(\mathbf{r}), t_z(\mathbf{r}) \le t_{max}, \tag{13}$$

$$C_{min} \le C(\mathbf{r}) \le C_{max}, \tag{14}$$

where $t_x(\mathbf{r})$, $t_y(\mathbf{r})$ and $t_z(\mathbf{r})$ denote the periodic variables along x, y, z axes respectively, $C(\mathbf{r})$ represents the thickness variable which satisfies the printing minimal thickness constraint, and $V(t_x(\mathbf{r}), t_y(\mathbf{r}), t_z(\mathbf{r}), C(\mathbf{r}))$ and V_0 represent the volume fraction of the optimized structure and a predefined threshold. The inequality (11) is the overhang constraints defined on surface points by the printing tolerance angle α_0, and (12) is the static equilibrium equation. The inequalities (13) and (14) are constraints for the design variables $t_x(\mathbf{r})$, $t_y(\mathbf{r})$, $t_z(\mathbf{r})$, $C(\mathbf{r})$.

The value ρ_i of the sign distance field ϕ_{opt} at $\mathbf{r_i} \in \Omega_M$ is calculated by (5) as:

$$\rho_i = 2C - \sqrt{2C^2 + 2\varphi^2(t_x(\mathbf{r}_i), t_y(\mathbf{r}_i), t_z(\mathbf{r}_i))}, \tag{15}$$

Thus, the density distribution $\overline{\rho}_i$ can be truncated by ρ_i:

$$\overline{\rho}_i = \begin{cases} 0, & \rho_i < 0; \\ 1, & \rho_i \ge 0. \end{cases} \tag{16}$$

To obtain a differentiable variable $\bar{\rho}_i$, (16) is replaced by its continuous approximation [18]:

$$\widetilde{\rho}_i = H_\xi(\rho_i) = \begin{cases} 1, & \rho_i > \xi; \\ \frac{1}{2}\left(\frac{\rho_i}{\xi} - \frac{\rho_i^3}{3\xi^3}\right) + \frac{1}{2}, & -\xi \le \rho_i \le \xi; \\ 0, & \rho_i < -\xi. \end{cases} \tag{17}$$

where ξ is the parameter that controls the magnitude of regularization. Based on our experience, we typically recommend ξ to be within the range of [0.04, 0.15]. Within this range, the optimized structures exhibit similar physical properties, and the choice of ξ can be adjusted depending on the specific design requirements. In our implementation, we set $\xi = 0.15$.

4.2. Fabrication constraints

4.2.1. Overhang constraints

The main goal of current work is to optimize the interior structure of an object such that it is self-supported as much as possible. Thus we need to handle overhang constraints.

Overhang regions in additive manufacturing are defined by the subtended angle [37] which is the angle between the printing direction $\mathbf{n}_p$ and the normal vector of a boundary point, as shown in Fig. 4(a). A surface point is considered unprintable if the subtended angle α exceeds the user-defined threshold α_0 (= $\frac{3\pi}{4}$). Boundary points with $\alpha \le \alpha_0$ are considered self-supported (marked by blue), and otherwise the surface points (marked by red) are overhanging points which require material support, as illustrated in Fig. 4(b).

Explicit overhang constraints. In our case, TPMS is defined in the interior of an object and may stretch and deform due to varying local frequencies and amplitudes. This may yield overhang parts during fabrication, as illustrated in Fig. 4(c). In this work, the surface points $\mathbf{r}^* = \{\mathbf{r}_k^*\}_{k=1}^M$ of the TPMS-based porous structure are extracted by the marching cube method [53] from ϕ_{opt}, as shown in Fig. 4(d). Where M is the number of surface

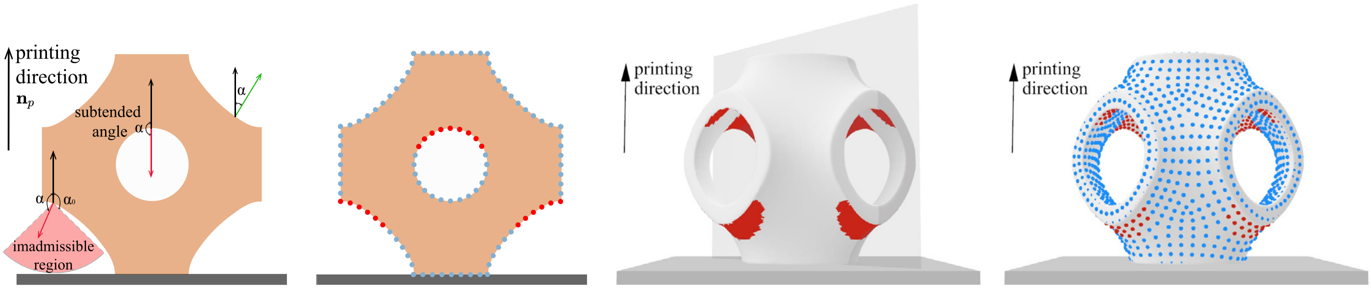

(a) Subtended angle (b) Boundary points $\mathbf{r}^*$ (c) Overhang regions (d) Surface points $\mathbf{r}^*$

Fig. 4. Illustration of overhang constraints. (a) Subtended angle. (b) Boundary points (red points are unprintable points and blue points are printable points). (c) Overhang regions. (d) Surface points of the model. (For interpretation of the references to color in this figure legend, the reader is referred to the web version of this article.)

points The normal of each point $\mathbf{n}_\phi(\mathbf{r}_k^*)$ can be easily computed according to the implicit representation ϕ_{opt} in (5). In order to be self-supported, a surface point $\mathbf{r}_k^*$ must obey the rule:

$$\alpha(\mathbf{r}_k^*) \leq \alpha_0, \quad \forall \bar{k}; \tag{18}$$

or equivalently,

$$\begin{aligned} A(\mathbf{r}_k^*) = \frac{\cos(\alpha(\mathbf{r}_k^*))}{\cos(\alpha_0)} &= \frac{\mathbf{n}_\phi(\mathbf{r}_k^*) \cdot \mathbf{n}_p}{\left\|\mathbf{n}_\phi(\mathbf{r}_k^*)\right\| \left\|\mathbf{n}_p\right\| \cos\alpha_0} \\ &= \frac{n_{\phi z}(\mathbf{r}_k^*)}{\left\|\mathbf{n}_\phi(\mathbf{r}_k^*)\right\| \cos\alpha_0} \leq 1, \quad \forall \bar{k}; \end{aligned} \tag{19}$$

where $\mathbf{n}_\phi = (n_{\phi x}, n_{\phi y}, n_{\phi z})$ is the normal vector of the boundary surface at point $\mathbf{r}_k^*$, $\mathbf{n}_p$ is the printing direction, and we set it to be the positive direction of the z-axis $(0, 0, 1)$. Notice that (19) clearly holds at surface point whose z-component of the normal vector is non-negative, i.e., $n_{\phi z} \geq 0$. Thus, we only need to consider the constraints (19) at the surface points $\mathbf{r}^{*-} = \{\mathbf{r}_k^*\}_{k=1}^N$ with $n_{\phi z} < 0$, where N is the number of surface points with a negative z-component of the normal vector.

However, it is very inefficient to directly impose the overhang constraints (19) during the optimization process. The reasons are twofold:

- The overhang constraints (19) are nonlinear. A large number of nonlinear constraints causes the optimization very inefficient.
- Imposing the overhang constraints on every point of the boundary surface is too strict. In fact, additional support structures are not needed in small overhang regions. Therefore, the overhang constraints corresponding to these points can be removed. Fig. 5 illustrates removable overhang regions in a model.

Modified overhang constraints. To overcome the first challenge, we integrate a large number of overhang constraints (19) into one global constraint:

$$A_g = \frac{1}{N}\sum_{k=1}^{N} g\left(\frac{n_{\phi z}(\mathbf{r}_k^*)}{\left\|\mathbf{n}_\phi(\mathbf{r}_k^*)\right\| \cos\alpha_0}\right) \leq 1 + \epsilon, \tag{20}$$

where N is the number of surface points with a negative z-component of the normal vector, and ϵ is a small positive value for the relaxation purpose. In our implementation, $\epsilon = 0.05$ is adopted. The function $g(x)$ is employed to penalize the quantity $A(\mathbf{r}_k^*)$ when $A(\mathbf{r}_k^*) > 1$ and is defined as:

$$g(x) = \begin{cases} (x-1)^2 + 1, & x \geq 1; \\ 1, & x < 1. \end{cases} \tag{21}$$

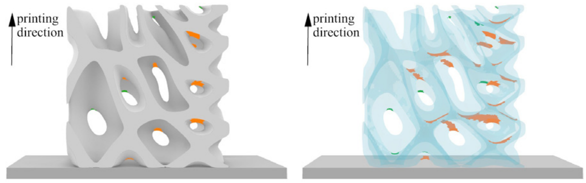

(a) A sectional view of overhang regions (b) Perspective view of overhang regions

Fig. 5. Removable small overhang regions. All the overhang regions are colored in the model, green regions represent small overhang regions that can be removed and orange regions represent actual overhang regions. (For interpretation of the references to color in this figure legend, the reader is referred to the web version of this article.)

In order to handle the second challenge, we introduce a filtering operation of small overhang regions by weighting a small area filtering function $w(\mathbf{r}^*)$ to the hanging constraints at surface points $\mathbf{r}^{*-} = \{\mathbf{r}_k^*\}_{k=1}^N$. Then the global constraint (20) is modified as:

$$\tilde{A}_g = \sum_{k=1}^{N} \tilde{w}(\mathbf{r}_k^*) g\left(\frac{n_{\phi z}(\mathbf{r}_k^*)}{\left\|\mathbf{n}_\phi(\mathbf{r}_k^*)\right\| \cos\alpha_0}\right) \leq 1 + \epsilon, \tag{22}$$

where $\tilde{w}(\mathbf{r}_k^*)$ is the normalized weight function corresponding to the small area filtering function $w(\mathbf{r}_k^*)$:

$$\tilde{w}(\mathbf{r}_k^*) = \frac{w(\mathbf{r}_k^*)}{\sum_{i=1}^{N} w(\mathbf{r}_i^*)}, \tag{23}$$

and

$$w(\mathbf{r}_k^*) = \begin{cases} \dfrac{2}{1+e^{\frac{2(1-s(\mathbf{r}_k^*))}{\eta}}} + 1, & A(\mathbf{r}_k^*) > 1; \\ 1, & A(\mathbf{r}_k^*) \leq 1; \end{cases} \tag{24}$$

whose graph is plotted in Fig. 6 in case that $A(\mathbf{r}_k^*) > 1$.

The function $s(\mathbf{r}_k^*)$ represents the ratio of the overhang points in a neighborhood of point $\mathbf{r}_k^*$:

$$s(\mathbf{r}_k^*) = \frac{card(S_{cons}(\mathbf{r}_k^*, \delta))}{card(S(\mathbf{r}_k^*, \delta))}, \tag{25}$$

where $S(\mathbf{r}_k^*, \delta)$ is the set of points in a neighborhood of $\mathbf{r}_k^*$, that is, $S(\mathbf{r}_k^*, \delta) = \{\mathbf{r}^* \in \mathbf{r}^{*-} \mid |\mathbf{r}^* - \mathbf{r}_k^*| \leq \delta\}$, $S_{cons}(\mathbf{r}_k^*, \delta)$ is the set of overhang points in the neighborhood $S(\mathbf{r}_k^*, \delta)$, that is, $S_{cons}(\mathbf{r}_k^*, \delta) = \{\mathbf{r}^* \in S(\mathbf{r}_k^*, \delta) \mid A(\mathbf{r}^*) > 1\}$, $\delta > 0$ is the radius of the neighborhood ball, and $card(S)$ represents the number of points in the set S. The parameter η in $w(\mathbf{r}_k^*)$ is related to the size of a removable region and will be discussed in section 5.3.2.

Fig. 7 illustrates the geometric meaning of $s(\mathbf{r}_k^*)$. The yellow points are the overhang points which we deal with. The green

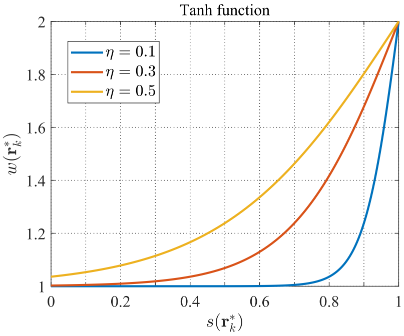

Fig. 6. The small area filtering function with different parameters.

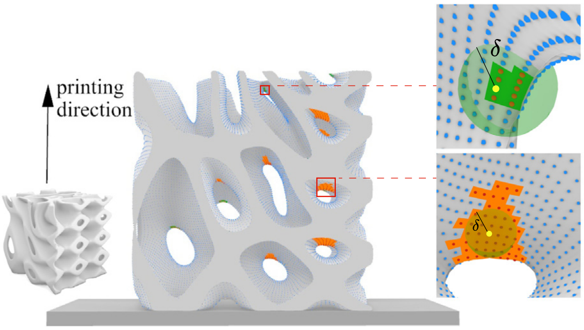

Fig. 7. Illustration of small area filtering functions. (For interpretation of the references to color in this figure legend, the reader is referred to the web version of this article.)

balls show the corresponding neighborhood of points $\mathbf{r}_k^*$. Removable small overhang regions are colored green and actual overhang regions are colored orange as before. From the zoom views on the right, we can see that $s(\mathbf{r}_k^*)$ in the actual overhang region has a large value while $s(\mathbf{r}_k^*)$ is small in the green region.

Based on the definition of small area filtering function $w(\mathbf{r}^*)$, self-supporting points and overhang points on the removable overhang regions have a small weight. On one hand, this operation filters out small overhang areas that can be printed, and on the other hand, it helps to reduce the number of large overhang regions in the optimization process.

4.2.2. Minimal thickness constraints

Additive manufacturing requires a minimum thickness of printed objects. When the size of a part of the printed model is smaller than the printable size of a printer, the part of the model will be unprintable.

To incorporate minimal thickness constraints into the optimization process, Guest [47] suggested performing a thickness-dependent projection of the density field to prevent the occurrence of structures smaller than the prescribed minimal thickness. In our model, the thickness of a structure is determined by the period variables $t_x(\mathbf{r}), t_y(\mathbf{r}), t_z(\mathbf{r})$ and the thickness variable $C(\mathbf{r})$ while $C(\mathbf{r})$ intuitively controls the thickness of the model as illustrated in Fig. 3. According to the homogenization method [14], we know that the stiffness of a periodic structure is scale-invariant in a unit volume. The effect of period variables is similar to scale transformation which also influences the thickness of the geometry. Fig. 8 shows that the minimal thickness varies with the variables $C(\mathbf{r})$ and $t_z(\mathbf{r})$ almost linearly. Therefore we impose linear constraints (13) and (14) for the variables $t_x(\mathbf{r}), t_y(\mathbf{r}), t_z(\mathbf{r})$ and $C(\mathbf{r})$. The choice of the parameter bounds t_{min}, t_{max} and C_{min}, C_{max} will be discussed in Section 5.3.1.

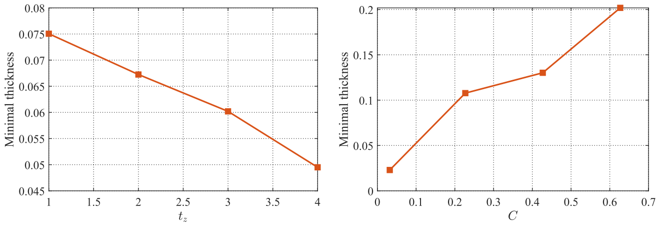

Fig. 8. Influence of the variables $t_z(\mathbf{r})$ and $C(\mathbf{r})$ on the minimal thickness of TPMS-based porous structures. The model is the same as that shown in Fig. 3.

4.3. Reformulation

To compute the optimization problem $(\mathcal{P})$, we should change the variables $t_x(\mathbf{r}), t_y(\mathbf{r}), t_z(\mathbf{r})$ and $C(\mathbf{r})$ into discrete forms by using the technique in Section 3.3. Then the discrete optimization problem takes the form:

$$(\mathcal{Q}): \quad \min_{t_x(\mathbf{r}_i), t_y(\mathbf{r}_i), t_z(\mathbf{r}_i), C(\mathbf{r}_i)} \quad \mathbf{I} = \mathbf{U}^{\mathbf{T}}\mathbf{F} \tag{26}$$

$$\text{s.t.} \quad V(t_x(\mathbf{r}_i), t_y(\mathbf{r}_i), t_z(\mathbf{r}_i), C(\mathbf{r}_i)) \leq V_0, \tag{27}$$

$$\tilde{A}_g = \sum_{k=1}^{N} \tilde{w}(\mathbf{r}_k^*) g\left(\frac{n_{\phi z}(\mathbf{r}_k^*)}{\left\|\mathbf{n}_\phi(\mathbf{r}_k^*)\right\| \cos\alpha_0}\right) \leq 1 + \epsilon, \tag{28}$$

$$\mathbf{KU} = \mathbf{F}, \tag{29}$$

$$t_{min} \leq t_x(\mathbf{r}_i), t_y(\mathbf{r}_i), t_z(\mathbf{r}_i) \leq t_{max}, \tag{30}$$

$$C_{min} \leq C(\mathbf{r}_i) \leq C_{max}, \tag{31}$$

where $\{\mathbf{r}_i\}_{i=1}^n$ are a set of collocation points that are evenly arranged in space. The numerical method to solve the optimization problem $(\mathcal{Q})$ will be discussed in the next subsection.

4.4. Numerical implementation

The optimization problem $(\mathcal{Q})$ can be solved by the Method of Moving Asymptotes (MMA) [54] which is widely used in topology optimization. MMA is an iterative approach to solve a general optimization problem. In each iteration step, an explicit subproblem is generated to approximate the original problem, and then the subproblem is solved by the primal–dual interior point method. The iteration process terminates until the termination conditions are satisfied.

To apply MMA to the optimization problem $(\mathcal{Q})$, we need to carry out finite element analysis of elasticity, i.e., to solve the static equilibrium Eq. (29) to update the variables in each iteration step. It involves computing the stiffness matrix $\mathbf{K}$ and solving a large and sparse linear system of equations $\mathbf{KU} = \mathbf{F}$, which is quite time-consuming. In the following, we present strategies to solve the linear system more efficiently.

***Computing stiffness matrix* K.** To start the finite element analysis, we first generate a conservative voxelized model from the given model Ω_M. This voxelized model can avoid remeshing in every iteration. We apply the super element strategy [55] by dividing the regular hexahedra elements (super elements) into smaller hexahedral elements (background elements) to improve the accuracy of FEM computation. The stiffness matrix is assembled on the background elements while the FEM computation is performed on the super element. As demonstrated in [55], the super element strategy provides better performance and convergence rates than traditional FEM calculations at the same resolution with background elements. To validate the effectiveness of our approach, we tested it on a cube model with

$50 \times 50 \times 50$ (4^3) elements (divide each super element into 4^3 background elements.), as well as on models with resolutions of $200 \times 200 \times 200$ elements. The results showed that this approach achieved a significant reduction in computation time, with runtimes of 10 s and 3560 s, respectively.

The stiffness matrix of super element $\bar{i}$ can be calculated as:

$$\begin{aligned}\mathbf{K}_{\bar{i}} &= \int_{\Omega_{\bar{i}}} \mathbf{B}^T \mathbf{D}_{\bar{i}} \mathbf{B} dV = \sum_{\bar{j}=1}^{n_b} \int_{\Omega_{\bar{i}\bar{j}}} \mathbf{B}^T \mathbf{D}_{\bar{i}} \mathbf{B} dV \\ &\approx \sum_{\bar{j}=1}^{n_b} E_{\bar{i}\bar{j}} \mathbf{B}_{\bar{i}\bar{j}}^T \mathbf{D}_0 \mathbf{B}_{\bar{i}\bar{j}} v_{\bar{i}\bar{j}} = \sum_{\bar{j}=1}^{n_b} E_{\bar{i}\bar{j}} \mathbf{K}_{\bar{i}\bar{j}}^0\end{aligned} \tag{32}$$

where $\Omega_{\bar{i}}$ denotes the $\bar{i}$th super element, $\Omega_{\bar{i}\bar{j}}$ denotes the $\bar{j}$th background element in the $\bar{i}$th super element, n_b is the number of background elements in a super element, $\mathbf{B}$ is the strain matrix, $\mathbf{D}_{\bar{i}}$ is the elastic matrix of $\Omega_{\bar{i}}$, $\mathbf{D}_0$ is the elastic matrix of the solid material, $v_{\bar{i}\bar{j}}$ is the volume of $\Omega_{\bar{i}\bar{j}}$ and $\mathbf{K}_{\bar{i}\bar{j}}^0 = \mathbf{B}_{\bar{i}\bar{j}}^T \mathbf{D}_0 \mathbf{B}_{\bar{i}\bar{j}} v_{\bar{i}\bar{j}}$ is the approximate integral of $\mathbf{B}^T \mathbf{D}_{\bar{i}} \mathbf{B}$ over $\Omega_{\bar{i}\bar{j}}$, In addition, $E_{\bar{i}\bar{j}}$ is the Young's modulus of the $\bar{j}$th background element in the $\bar{i}$th super element. In all the results presented in this paper, each super element is divided into 4^3 background elements.

The SIMP scheme [15] is adopted to model the Young's modulus $E_{\bar{i}\bar{j}}$:

$$E_{\bar{i}\bar{j}} = E_{min} + \widetilde{\rho}_{\bar{i}\bar{j}}^{p} (E_0 - E_{min}), \tag{33}$$

where $\widetilde{\rho}_{\bar{i}\bar{j}}$ is the density of the $\bar{j}$th background element in the $\bar{i}$th super element, E_0 is the Young's modulus of solid elements, $E_{min}\,(= 10^{-6})$ avoids calculation singularity, and $p\,(= 3)$ is the penalization power. Based on our experiments, we observe that the optimized structures have similar physical properties in terms of compliance and self-supporting ratio. Furthermore, optimized structures using different penalty factors (3, 4, 5) show comparable results.

Note that $\mathbf{K}_{\bar{i}\bar{j}}^0$ is the same for different super elements, so we only need to compute it once in one super element and store them as a template $\mathbf{K}^0$. In each iteration, we just compute $E_{\bar{i}\bar{j}}$ according to (33) to update $\mathbf{K}_{\bar{i}}$.

Acceleration. Iterative methods such as Gauss–Seidel relaxation can be used to solve the linear system of (29) in principle. However, the convergence of such methods is generally slow, especially under high resolutions. Here we propose to employ the multigrid method [56] to accelerate the computation. But linear elasticity multigrid solvers for large problems are memory bound, meaning that they operate close to the theoretical memory bandwidth and further performance increases are difficult to achieve. To address this limitation, Dick et al. [57] proposed a GPU multigrid implementation which exploits the fast memory interface on such architectures. We adopt this multigrid technique based on GPU in our implementation. It has a parallelization scheme and matrix-free data structure, and significant performance improvements were reported compared to a CPU implementation. We have tested the effectiveness of the multigrid method in solving a set of finite element equations with a scale of 50^3. It appears that there is a significant reduction in the time required for each iteration, with the time decreasing from 1633 s to just a few seconds.

Our optimization process, which involves finite element analysis, sensitivity analysis, and MMA, is implemented on the GPU using the CUDA parallel programming API. Based on our experimental tests, GPU computing reduced the runtime by approximately 90% and the memory consumption by around 80% compared with CPU computing.

Volume discretization. In order to solve the optimization problem ($\mathcal{Q}$), the volume in the constraint (27) should be calculated. This can be done by discretizing the volume as:

$$\frac{1}{8} \sum_{j=1}^{N_b} \sum_{l=1}^{8} \widetilde{\rho}_l^j v_b, \tag{34}$$

where $\widetilde{\rho}_l^j$ is the density at lth node point of the jth background element and is computed according to the Eqs. (15)–(17), and N_b is the total number of background elements.

Two-stage optimization. To expedite the optimization process for the problem ($\mathcal{Q}$) while using MMA, which typically exhibits slow convergence and longer optimization time, we divide it into two stages: ***period optimization*** and ***thickness optimization***. During the period optimization stage, we keep the variables $C(\mathbf{r}_i)$ fixed and treat $t_x(\mathbf{r}_i)$, $t_y(\mathbf{r}_i)$, and $t_z(\mathbf{r}_i)$ as optimization variables. Conversely, during the thickness optimization stage, we fix $t_x(\mathbf{r}_i)$, $t_y(\mathbf{r}_i)$, and $t_z(\mathbf{r}_i)$ and treat $C(\mathbf{r}_i)$ as the optimization variables. This approach helps to achieve faster convergence and reduces the overall optimization time by half.

The input of our system is a model Ω_M represented by a surface mesh. The system first computes a voxelized model. Then the voxel model is optimized with two-stage optimization. The termination criteria for each optimization stage is expressed as:

$$\begin{aligned}&\frac{\|I - I^{avg}|}{I^{avg}} \le 1 \times 10^{-3}, \\ &\frac{\|V - V^{avg}\|}{V^{avg}} \le 1 \times 10^{-3}, \\ &\frac{\|\tilde{A}_g - \tilde{A}_g^{avg}\|}{\tilde{A}_g^{avg}} \le 1 \times 10^{-3},\end{aligned} \tag{35}$$

where I, V and $\tilde{A}_g$ are the compliance, the volume fraction and the function defined in (22) in the current iteration, respectively. I^{avg}, V^{avg} and $\tilde{A}_g^{avg}$ are the average values of I, V and $\tilde{A}_g$ in the last ten iterations, respectively. Once the constraints have been satisfied and the two-stage optimization has converged, the final structure is generated.

4.5. Sensitivity analysis

In this subsection, we perform a sensitivity analysis of the objective function and the constraints with respect to the design variables.

Period optimization. In this process, we fix the thickness variables $\{C_i\}_{i=1}^n$ and calculate the sensitivity analysis with respect to the period variables $\{t_{xi}\}_{i=1}^n$, $\{t_{yi}\}_{i=1}^n$ and $\{t_{zi}\}_{i=1}^n$.

$$\begin{aligned}\frac{\partial I}{\partial t_{xi}} &= -\mathbf{U}^T \frac{\partial K}{\partial t_{xi}} \mathbf{U} \\ &= -\sum_{\bar{i}=1}^{N_s} \mathbf{U}_{\bar{i}}^T \left(\frac{1}{8} \sum_{\bar{j}=1}^{n_b} \left(\sum_{l=1}^{8} \frac{\partial H_\xi \left(\rho_l^{\bar{i}\bar{j}} \right)}{\partial t_{xi}} \right) \mathbf{K}^0 \right) \mathbf{U}_{\bar{i}}, \\ \frac{\partial V}{\partial t_{xi}} &= \frac{1}{8} \sum_{j=1}^{N_b} \sum_{l=1}^{8} \frac{\partial H_\xi \left(\rho_l^j \right)}{\partial t_{xi}} v_j, \\ \frac{\partial \tilde{A}_g}{\partial t_{xi}} &= \sum_{k=1}^{N} \tilde{w}(\mathbf{r}_k^*) g' \left(\frac{n_{\phi z}(\mathbf{r}_k^*)}{\left\| \mathbf{n}_\phi(\mathbf{r}_k^*) \right\| \cos\alpha_0} \right) \\ &\quad \left(\frac{\frac{\partial n_{\phi z}(\mathbf{r}_k^*)}{\partial t_{xi}} \|\mathbf{n}_\phi(\mathbf{r}_k^*)\| - n_{\phi z}(\mathbf{r}_k^*) \frac{\partial \|\mathbf{n}_\phi(\mathbf{r}_k^*)\|}{\partial t_{xi}}}{\|\mathbf{n}_\phi(\mathbf{r}_k^*)\|^2 \cos\alpha_0} \right),\end{aligned} \tag{36}$$

where N_s and N_b are the total numbers of super elements and background elements in the model, respectively, n_b is the number of background elements in a super element, and $\rho_l^{\bar{i}\bar{j}}$ represents density at the lth node point of the $\bar{j}$th background element in the $\bar{i}$th super element. ρ_l^j is density of the lth node point of the jth background element in the model and v_j is the volume of jth background element in the whole model. The sensitivity analysis with respect to $\{t_{yi}\}_{i=1}^n$ and $\{t_{zi}\}_{i=1}^n$ can be computed in a similar way.

The derivatives of H_ξ, $n_{\phi z}(\mathbf{r}_\mathbf{k}^*)$ and $\|\vec{n}_\phi(\mathbf{r}_\mathbf{k}^*)\|$ are computed by applying the chain rule, i.e.,

$$\begin{aligned}
\frac{\partial H_\xi\left(\rho_l^{\bar{i}\bar{j}}\right)}{\partial t_{xi}} &= \frac{\partial H_\xi\left(\rho_l^{\bar{i}\bar{j}}\right)}{\partial \rho_l^{\bar{i}\bar{j}}} \frac{\partial \rho_l^{\bar{i}\bar{j}}}{\partial t_x} \frac{\partial t_x}{\partial t_{xi}}, \\
\frac{\partial n_{\phi z}(\mathbf{r}_k^*)}{\partial t_{xi}} &= \frac{\partial n_{\phi z}(\mathbf{r}_k^*)}{\partial t_x} \frac{\partial t_x}{\partial t_{xi}}, \\
\frac{\partial \|\mathbf{n}_\phi(\mathbf{r}_k^*)\|}{\partial t_{xi}} &= \frac{\mathbf{n}_\phi(\mathbf{r}_k^*)}{\|\mathbf{n}_\phi(\mathbf{r}_k^*)\|} \cdot \left(\frac{\partial n_{\phi x}(\mathbf{r}_k^*)}{\partial t_{xi}}, \frac{\partial n_{\phi y}(\mathbf{r}_k^*)}{\partial t_{xi}}, \frac{\partial n_{\phi z}(\mathbf{r}_k^*)}{\partial t_{xi}}\right),
\end{aligned} \tag{37}$$

where t_x can be computed according to Eqs. (7) and (8).

Thickness optimization. In this process, we fix the period variables and optimize the thickness variables $\{C_i\}_{i=1}^n$. The sensitivity analysis is calculated as:

$$\begin{aligned}
\frac{\partial I}{\partial C_i} &= -\mathbf{U}^T \frac{\partial K}{\partial C_i} \mathbf{U} \\
&= -\sum_{\bar{i}=1}^{N_s} \mathbf{U}_{\bar{i}}^T \left(\frac{1}{8} \sum_{\bar{j}=1}^{n_b} \left(\sum_{l=1}^{8} \frac{\partial H_\xi\left(\rho_l^{\bar{i}\bar{j}}\right)}{\partial C_i}\right) \mathbf{K}^0\right) \mathbf{U}_{\bar{i}}, \\
\frac{\partial V}{\partial C_i} &= \frac{1}{8} \sum_{j=1}^{N_b} \sum_{l=1}^{8} \frac{\partial H_\xi\left(\rho_l^j\right)}{\partial C_i} v_j, \\
\frac{\partial \tilde{A}_g}{\partial C_i} &= \sum_{k=1}^{M} \tilde{w}(\mathbf{r}_k^*) g'\left(\frac{n_{\phi z}(\mathbf{r}_k^*)}{\|\mathbf{n}_\phi(\mathbf{r}_k^*)\| \cos\alpha_0}\right) \\
&\quad \left(\frac{\frac{\partial n_{\phi z}(\mathbf{r}_k^*)}{\partial C_i} \|\mathbf{n}_\phi(\mathbf{r}_k^*)\| - n_{\phi z}(\mathbf{r}_k^*) \frac{\partial \|\mathbf{n}_\phi(\mathbf{r}_k^*)\|}{\partial C_i}}{\|\mathbf{n}_\phi(\mathbf{r}_k^*)\|^2 \cos\alpha_0}\right).
\end{aligned} \tag{38}$$

5. Results and discussion

This section demonstrates the performance of our proposed structure optimization algorithm for different models. P surfaces are adopted as the TPMS representation in the porous structure optimization. The algorithm is implemented in C++ and runs on a PC with 3.20 GHz Intel(R) Core(TM) i7-8700 and 64 GB memory.

5.1. Pipeline

For a given model, we first generate a bounding box to enclose the input model and scale the bounding box such that the length of the longest edge of the bounding box is 1. The size of the bounding box will affect the selection of period parameters. In fact, if the bounding box is scaled by a factor κ, then the period parameters will be scaled by $1/\kappa$. After the bounding box is calculated, the system computes a voxelized model which is optimized with the two-stage optimization process introduced in the previous section. Once the constraints are satisfied and the two-stage optimization has converged, the final structure is generated. The overall optimization algorithm is described in Algorithm 1. Fig. 9 shows sliced views of a model and the physical properties (compliance, volume fraction and self-supporting ratio) along with the period and thickness optimization processes.

Algorithm 1 Fabrication friendly TPMS-based porous structure optimization

```
Input: A model $\Omega_M$, forces $F$, fixed area $\Gamma_u$
Output: Period and thickness parameters
Generate a conservative voxelized domain from $\Omega_M$
Generate a set of collocation points
Initialize $\{t_{xi}\}_{i=1}^n$, $\{t_{yi}\}_{i=1}^n$, $\{t_{zi}\}_{i=1}^n$, $\{C_i\}_{i=1}^n$ at the collocation points
$h \leftarrow 1$
while $h < max\_iter$ && $!converged$ do
    Update the combinatorial coefficients in (7)
    Generate a set of surface points $\{\mathbf{r}_k^*\}_{k=1}^M$ by the marching cube method
    Solve the linear system $\mathbf{KU} = \mathbf{F}$ by the multigrid method to obtain $\mathbf{U}$
    Compute $I$, $V$, $\tilde{A}_g$ and perform sensitivity analysis $\frac{\partial I}{\partial t_{xi}}$, $\frac{\partial V}{\partial t_{xi}}$, $\frac{\partial \tilde{A}_g}{\partial t_{xi}}$, $\frac{\partial I}{\partial t_{yi}}$, $\frac{\partial V}{\partial t_{yi}}$, $\frac{\partial \tilde{A}_g}{\partial t_{yi}}$, $\frac{\partial I}{\partial t_{zi}}$, $\frac{\partial V}{\partial t_{zi}}$, $\frac{\partial \tilde{A}_g}{\partial t_{zi}}$
    Update period variables $\{t_{xi}\}_{i=1}^n$, $\{t_{yi}\}_{i=1}^n$, $\{t_{zi}\}_{i=1}^n$ by MMA
    $h \leftarrow h + 1$
    $converged \leftarrow check\_converge\_condition()$
end while
$h \leftarrow 1$
while $h < max\_iter$ && $!converged$ do
    Update the combinatorial coefficients in (7)
    Generate a set of surface points $\{\mathbf{r}_k^*\}_{k=1}^M$ by the marching cube method
    Solve the linear system $\mathbf{KU} = \mathbf{F}$ by the multigrid method to obtain $\mathbf{U}$
    Compute $I$, $V$, $\tilde{A}_g$ and perform sensitivity analysis $\frac{\partial I}{\partial C_i}$, $\frac{\partial V}{\partial C_i}$, $\frac{\partial \tilde{A}_g}{\partial C_i}$
    Update the thickness variables $\{C_i\}_{i=1}^n$ by MMA
    $h \leftarrow h + 1$
    $converged \leftarrow chech\_converge\_condition()$
end while
```

5.2. Performance

We choose four models–bunny, duck, kitten and molar as illustrated in Fig. 10(a) (the red arrows represent external forces imposed on the models) to test the performance of our structure optimization algorithm, and comparison results with two other models are also provided.

In order to show the effectiveness of our algorithm, we compare the results by our method with the results by two other models. One is the optimization model ($\mathcal{Q}$) without the overhang constraint (28), which is similar to the model proposed in [32]. The other is the initial model we set for solving the problem ($\mathcal{Q}$). We generate the initial model from the model with the same period variables $t_x = t_y = t_z = 4$, and then stretch the model in z direction by setting $t_z \in [1, 1.4]$ in order to satisfy self-supporting constraints as much as possible. Finally, we adjust the thickness variable C such that the volume constraint is satisfied. Fig. 10(b) shows the initial models generated by the above settings.

We compare the results by the following quantities: compliance, volume fraction, self-supporting ratio and computational time for four different models. All the models are tested with three different volume fractions 35%, 50% and 65%. The statistics are summarized in Fig. 11. From the picture we can observe that our algorithm effectively reduces the compliance of the initial models, which means the optimized structures have better stiffness than the initial models. As for the comparison with the traditional topology optimization with only the volume constraint

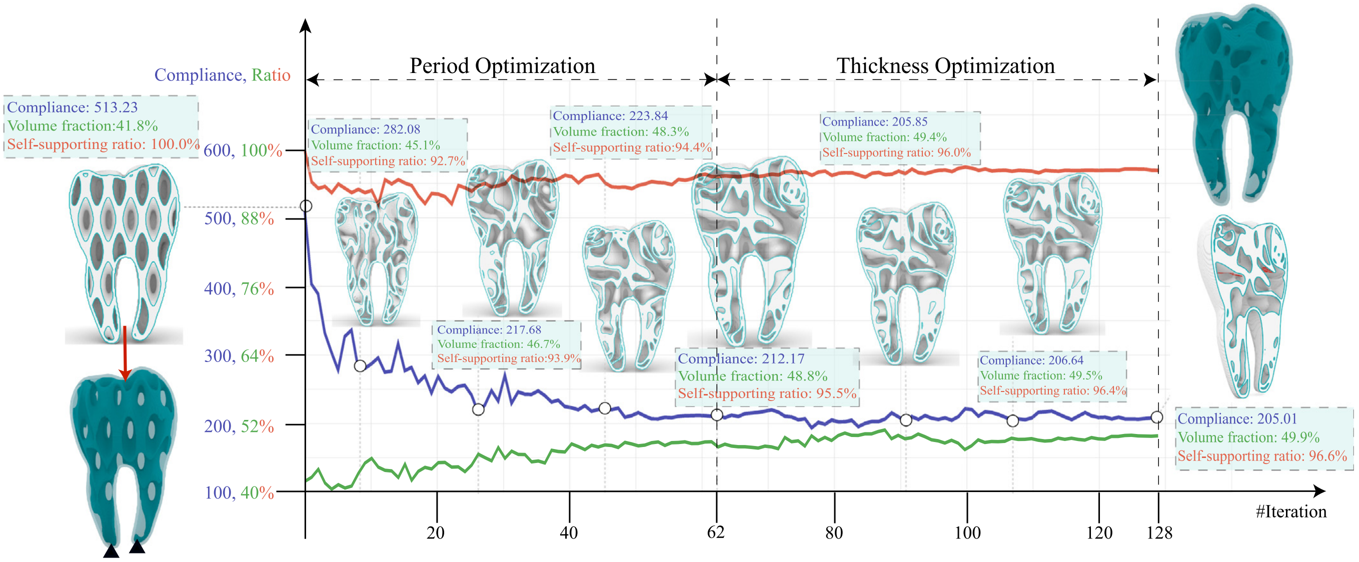

Fig. 9. Physical properties (compliance, volume fraction and self-supporting ratio) of the molar model during the optimization process. Blue, green and red curves represent compliance, volume fraction and self-supporting ratio respectively. (For interpretation of the references to color in this figure legend, the reader is referred to the web version of this article.)

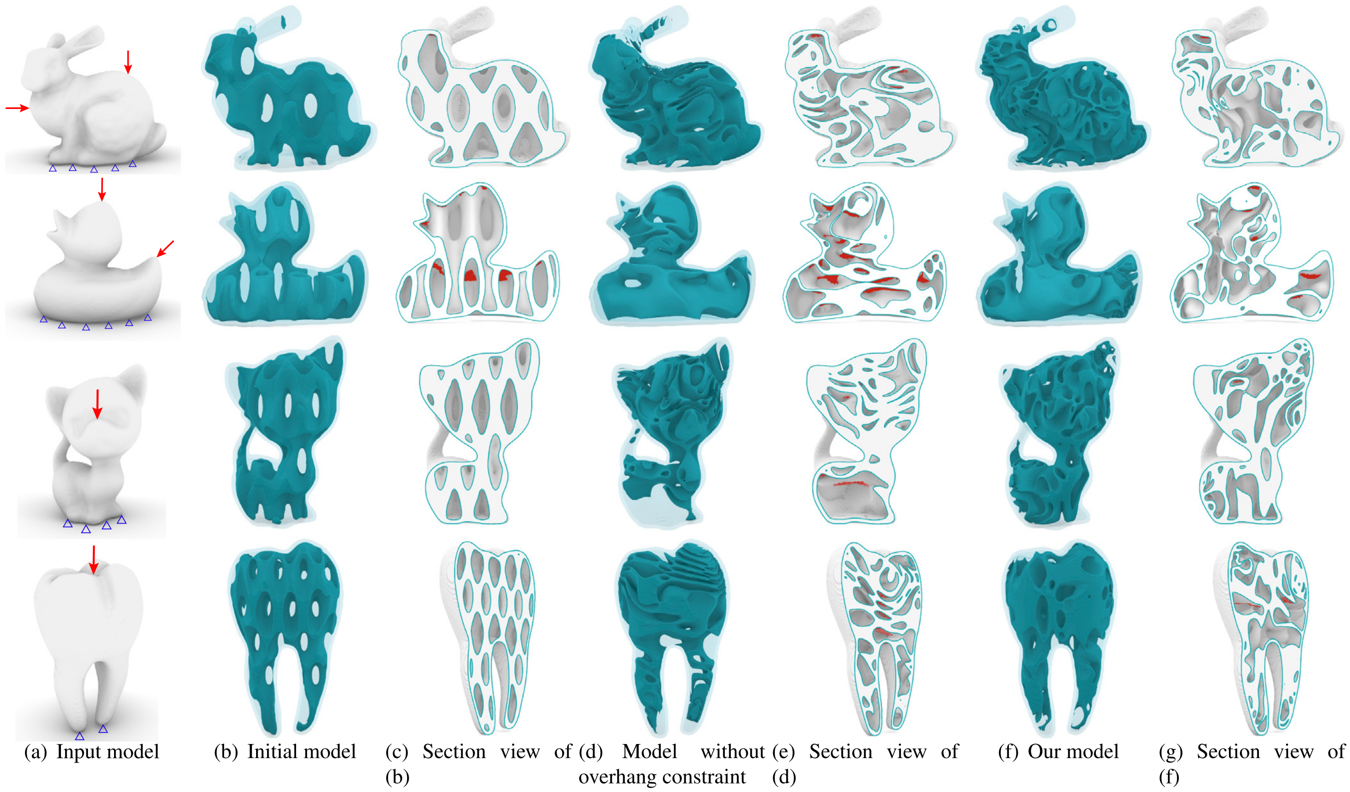
(a) Input model (b) Initial model (c) Section view of (b) (d) Model without overhang constraint (e) Section view of (d) (f) Our model (g) Section view of (f)

Fig. 10. Optimization of TPMS-based porous structures. (a) Input models with boundary conditions and external forces. (b)(d)(f) The structures of the initial model, the model without the overhang constraint and our model, respectively. (c)(e)(g) are the corresponding section views of (b)(d)(f). The overhang regions are colored in red. (For interpretation of the references to color in this figure legend, the reader is referred to the web version of this article.)

(e.g., the method in [32]), there is not much difference between the compliance. However, our method improves the average self-supporting ratio from 85% to 96%, which means that our models are more suitable for 3D printing. Furthermore, our method can also improve the printing accuracy, because 3D printers may change the structure a little bit when they encounter some unprintable areas. Figs. 10(d) and 10(f) show the results generated by the two methods respectively.

The computational performance of our algorithm is summarized in Table 1, where the second column lists the number of

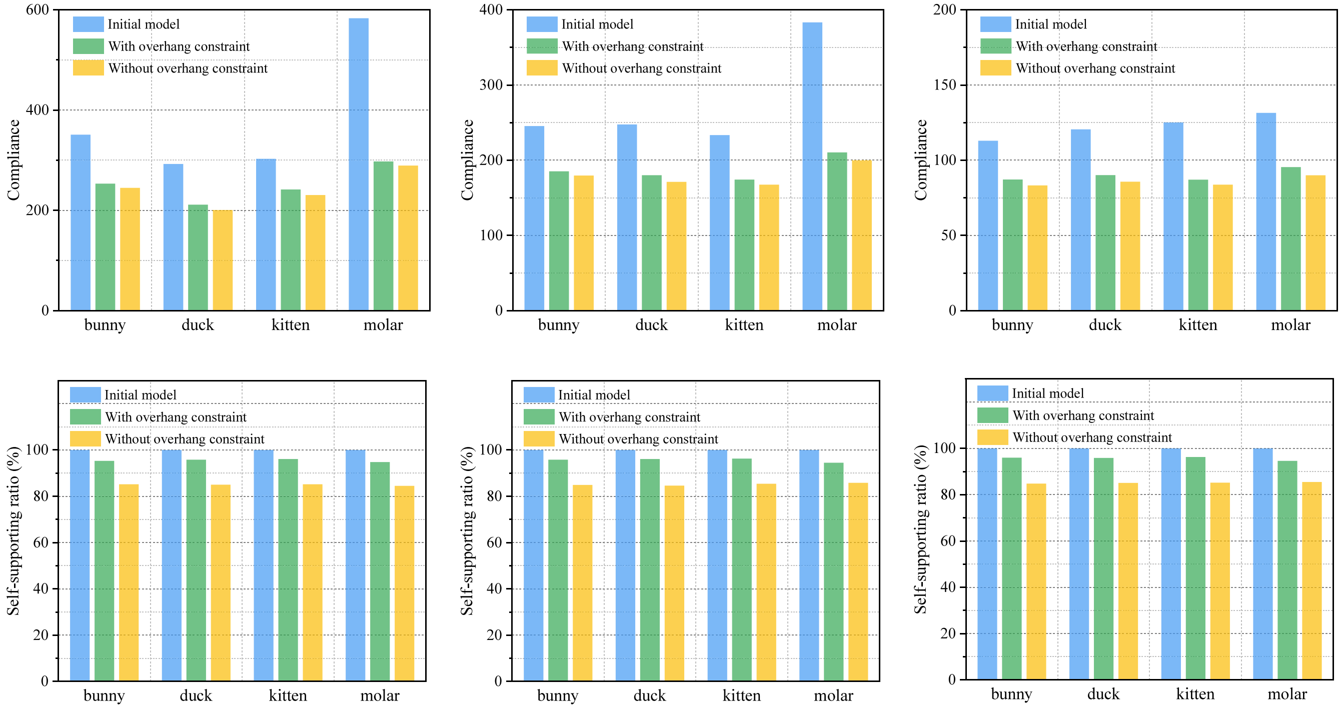

(a) Volume fraction = 35%

(b) Volume fraction = 50%

(c) Volume fraction = 65%

Fig. 11. Comparison results of porous structures for different volume fractions.

Table 1
Computational performance of two methods for different models.

Model	#Elements	Method	#Iter. (Period)	#Iter. (Thickness)	Time[min/iter] (Period)	Time[min/iter] (Thickness)	Total[min]
Bunny	6.24×10^6	Ours Without overhang constraint	54 58	26 33	1.93 1.67	1.52 1.29	143.74 139.43
Duck	5.91×10^6	Ours Without overhang constraint	49 55	47 45	2.04 1.70	1.65 1.33	177.51 153.35
Kitten	3.17×10^6	Ours Without overhang constraint	56 44	41 46	1.88 1.56	1.47 1.21	165.55 124.30
Molar	2.41×10^6	Ours Without overhang constraint	62 65	64 70	1.61 1.27	1.23 0.98	178.54 151.15

elements used in the finite element simulation, the four column shows the number of iterations in the two-stage optimization, and the last column is the total computational time. As we can see from the table, our porous structure optimization algorithm costs a little more overhead than the optimization without the self-supporting constraint. Yet our algorithm improves the supporting ratio by ten percent. On the other hand, the computational cost of our algorithm depends largely on the number of finite elements used in the analysis, and for models discretized into millions of elements, the computational time is less than three hours.

5.3. Discussion

In this section, we discuss the initialization and bound selection of the design variables. The choice of the parameter in the small area filtering function is also discussed.

5.3.1. Design variables

Period and thickness variables initialization. For different choice of the period and thickness variables, the resulting TPMS-based porous structures are quite different, as illustrated in the previous picture– Fig. 3. Fig. 13 further depicts how the compliance and the volume fraction of the initial model depend on the change of the design variables. From the pictures we can see that, while the volume fraction is proportional to the design variables, the compliance monotonically decreases as the design variables increase.

According to our experiment, for a fixed volume fraction, the compliances and self-supporting ratios of the optimized structures have little difference for different initializations of the design variables. However, the optimized structures vary with different initializations. Generally, the larger the initial period variables, the more complex the internal structure of the optimized model, as shown in the middle column (with a volume fraction of 50%) and the right column (with a volume fraction of 65%) in Fig. 12. Table 2 gives the corresponding numerical results of compliances and self-supporting ratios of the optimized structures. As we can observe, for a fixed volume fraction, the compliance and the self-supporting ratios of the optimized structures have little difference under different initializations of design variables. However, compliance depends mainly on volume fractions.

In [32], Hu et al. concluded that the minimal thickness of a TPMS is inversely proportional to the period variables and directly proportional to the thickness variable, and they gave an

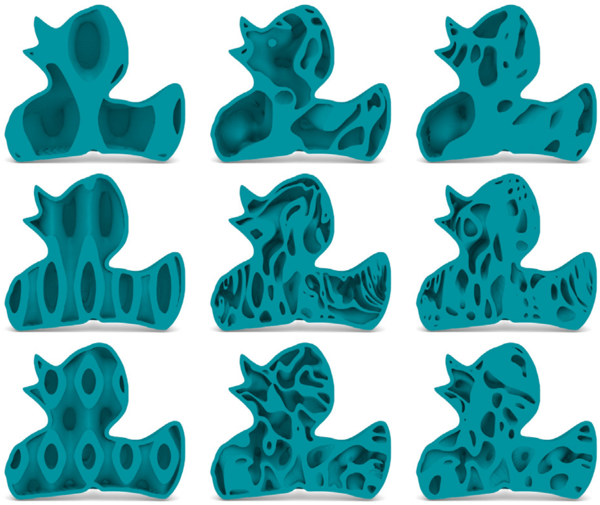

Fig. 12. Comparison of different period and thickness variable initializations. The left column shows the initial models, the middle and right columns are the corresponding optimized structures by our algorithm with a volume fraction 50% and 65% respectively.

Table 2
Statistic results of optimized porous structures for different initializations.

Initialization (t_x, t_y, t_z, C)	Volume	Compliance	Self-supporting ratio
Top(2, 2, 1, 0.5)	50% 65%	179.49 90.33	95.8% 95.9%
Middle(4, 4, 1, 0.5)	50% 65%	180.11 89.80	96.1% 96.2%
Bottom(4, 4, 2, 0.5)	50% 65%	181.01 90.76	95.9% 95.7%

estimation of the minimal thickness for the worst case:

$$\omega_{min} \approx \frac{0.1838C(\mathbf{r}_*)}{t(\mathbf{r}_*)}, \tag{39}$$

where ω_{min} (= 0.02 in our setting) is the minimal thickness at the location $\mathbf{r}_*$. Based on this formula, we can set the initial period variable t_0 and the thickness variable C_0 to satisfy the constraint:

$$\omega_{min} = \frac{0.1838C_0}{t_0}. \tag{40}$$

On the other hand, we can employ the relationship between the design variables and the compliance and volume fraction of the initial model (as illustrated in Fig. 13) to estimate upper bounds for t_0 and C_0. Then we combine the formula (40) to set t_0 and C_0 such that they are as large as possible in order to minimize the compliance.

Period and thickness variables bound setting. In the optimization problem ($\mathcal{Q}$), the bounds $t_{min}, t_{max}, C_{min}, C_{max}$ of the period and thickness variables have influence on the final results. First, the thickness variable $C(\mathbf{r})$ influences the minimal thickness and valid representation of the porous structure. Too small C_{min} would result in a too thin structure which is unprintable. On the other hand, too large C_{max} would result in a too thick structure which may have local and global self-intersections. According to our experiments, a reasonable choice is $C_{min} = 0.05$ and $C_{max} = 0.8$ for P surfaces. Next, we consider the bounds of the period variables $t_x(\mathbf{r})$, $t_y(\mathbf{r})$ and $t_z(\mathbf{r})$. Generally too small period would result in void solids and too large period would produce too complex structure. According to our experiment, we set $t_{min} = 0.28$. For the maximal period, we set it according to the following relation based on the formula (39):

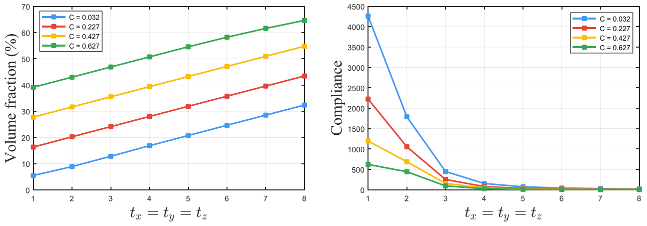

Fig. 13. Influence of the period variables and thickness variables on the volume fraction and compliance of the initial porous structure.

$$\omega_{min} \leq \frac{0.1838C_{max}}{t_{max}}, \tag{41}$$

and thus we set $t_{max} = 0.1838C_{max}/\omega_{min}$.

5.3.2. Small area filtering function

For an overhang region whose area is less than some tolerance A_{tol} (A_{tol} is set to be 16 mm × 16 mm in our implementation), we do not have to add any supporting material in 3D printing, that is, the region is considered as self-supporting. For the overhang regions whose areas are larger than A_{tol}, an overhang constraint must be imposed. For that purpose, a small area filtering function $w(\mathbf{r}_k^*)$ defined in (24) is constructed. The weight function $w(\mathbf{r}_k^*)$ has a relatively large value at overhang regions and a relatively small value at non-overhang regions.

To actually compute the function, we first generate a set of surface points of a porous structure by the marching cube method and label the overhang points. Then we compute the k-neighborhood points of every overhang point $\mathbf{r}_k^*$ to get the overhang ratio $s(\mathbf{r}_k^*)$ at this point. The radius δ of the neighborhood ball is set to be 0.01 in our experiment. Finally the overhang function can be computed according to (24).

In the formula (24) of the small area filtering function $w(\mathbf{r}_k^*)$, the parameter η is selected according to the threshold A_{tol}. Fig. 14 shows the effect of the parameter η on the overhang regions for the same model. We find that $\eta = 0.3$ gives a better self-supporting result according to our numerical experiment. Fig. 14 depicts the over-hang regions of the Kitten model for different parameter values of η.

5.4. Comparisons

Implementation details. Many previous works have considered overhang constraints in topology optimization for additive manufacturing such as [39,40,42]. We compare it with the representative work of Qian [39] in three aspects. Firstly, Qian et al. [39] took element density as design variables and density gradients to approximate boundary normals, while we used TPMS-based geometry by optimizing the period and thickness parameters. This allows us to generate complex and smooth geometries with high self-supporting ratios, and establish a correlation between print size and the thickness parameter in TPMS for better print quality. Secondly, we utilize acceleration techniques such as a super element strategy, a multigrid solver, and GPU computing

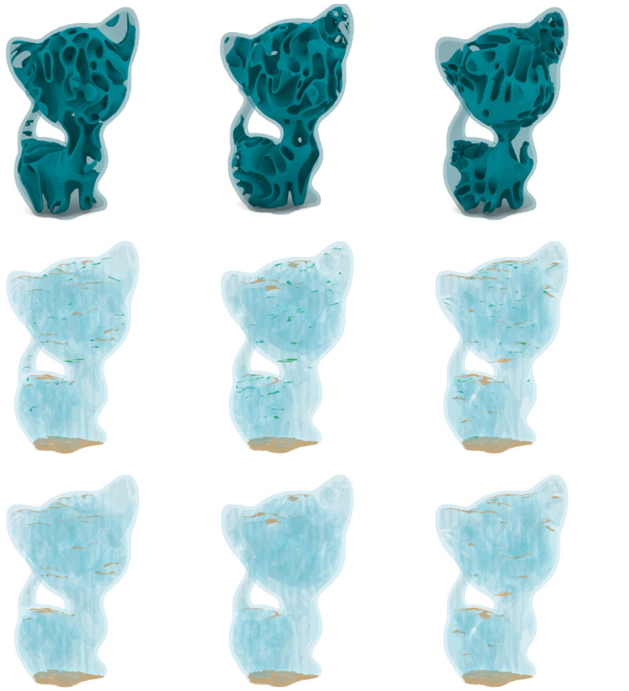
(a) $\eta = 0.1$ (b) $\eta = 0.3$ (c) $\eta = 0.5$

Fig. 14. Parameter setting in the small area filtering function. The top row is the optimized TPMS-based porous structures. The models in the middle row show the removable overhang regions and the actual overhang regions colored in green and orange, respectively. The bottom row shows the final overhang regions in the models. (For interpretation of the references to color in this figure legend, the reader is referred to the web version of this article.)

via the CUDA parallel programming API to handle millions of elements and achieve high-performance computing. This enables us to handle large-scale problems and obtain efficient solutions. Finally, our TPMS-based geometry generates smooth and connected porous structures instead of sharp features, which can occur in Qian [39]. This is essential for practical applications where smooth and connected geometries are preferred.

Von mises stress. There are numerous previous studies on optimizing infill structures using various methods, including support-free lattices [13,43], gyroids [31], and spheroids [44]. We have conducted a comparison of Von Mises stress, as shown in Fig. 15. The structures used for the comparison include honeycomb structures [58], uniform support-free infill structures [43], non-uniform support-free infill structures [13], as well as uniform TPMS-based support-free infill structures. The stress distribution analysis reveals that our model bears less stress under two volume fraction settings, and the maximum stress is the lowest among all the structures.

Compression tests. We conducted physical experiments to validate our results by fabricating the optimized structures using a Bambu X1-Carbon Combo 3D printer and subjecting it to compression testing. The models are printed using PLA, and we conduct compression testing on three sets of models: a kitten model, a duck model, and a bunny model with heights of 12 cm, 8 cm, and 8 cm, respectively. The MTS809 Axial/Torsional Test System is used to evaluate the strength of the printed models, as depicted in Fig. 16(a). The crosshead is moved at a constant speed of 2 mm/min, generating a consistent compressive force. The results shown in Fig. 16(b) demonstrate that our optimized structures can withstand significantly more force compared to the uniform support-free TPMS infill model used as the initialization.

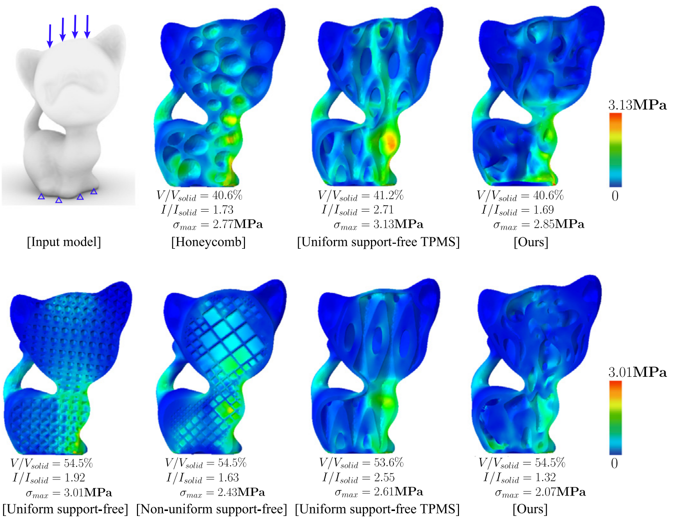

Fig. 15. Comparisons of Von Mises stress of different structures.

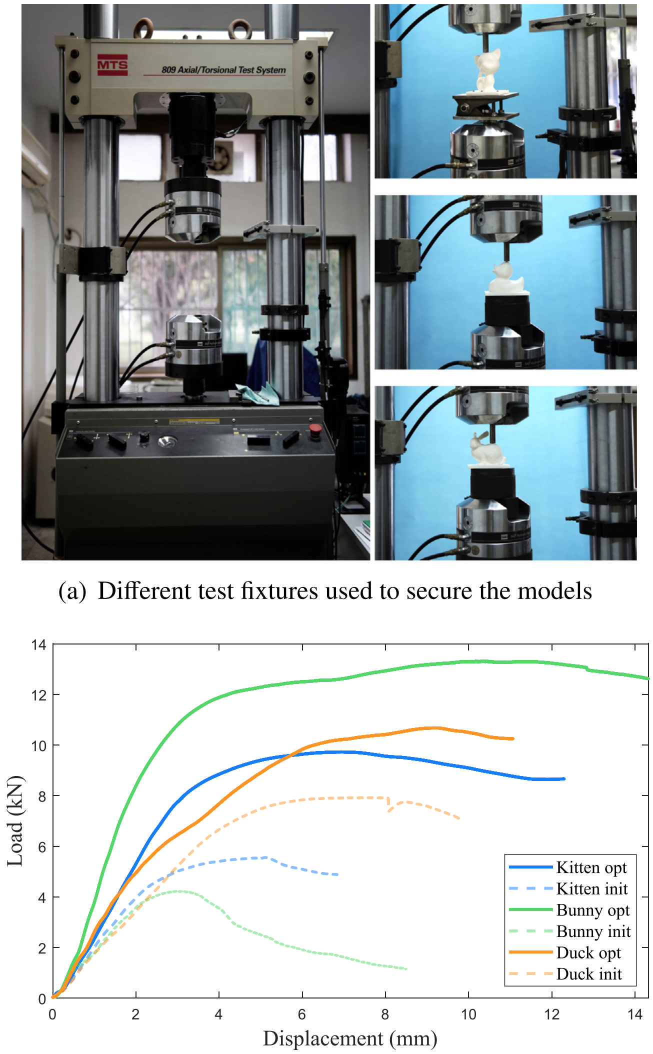

(a) Different test fixtures used to secure the models

(b) The displacement-load curves of different models

Fig. 16. Compression tests using MTS809 Axial/Torsional Test System.

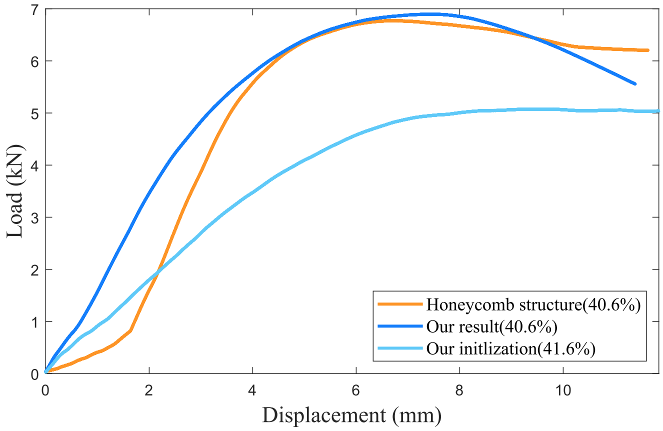

Fig. 17. The displacement–load curves of the physical tests for different methods of 40.6% volume fraction.

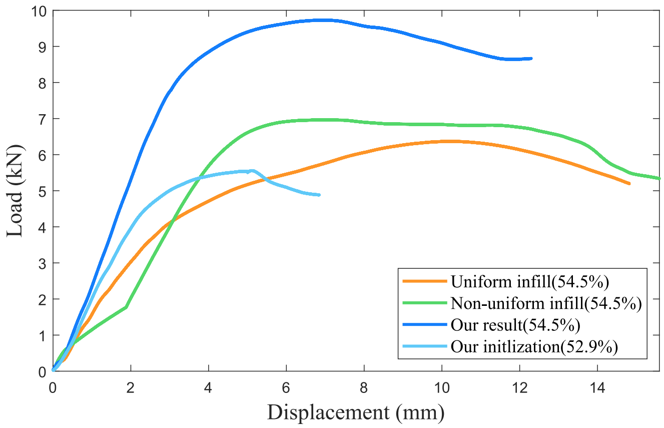

Fig. 18. The displacement–load curves of the physical tests for different methods of 54.5% volume fraction.

Furthermore, we have conducted compression tests on our structures and others shown in Fig. 15. The tests are conducted under two volume fraction settings, and the statistical results are plotted in Figs. 17 and 18. The results in Fig. 17 demonstrate that our optimized structure can withstand higher force compared to honeycomb structure models, while the honeycomb model does not take overhang constraints into consideration. Our optimized model with a 54.5% volume fraction can withstand nearly 10kN of force, with significantly better stiffness than models generated by other methods, as shown in Fig. 18. The detailed structures after compression tests are shown in Fig. 19.

Fabrication quality. To compare the printing results of our method with and without the self-supporting constraint, we print four optimized models shown in Fig. 10 with two methods (ours shown on the left vs structures optimized without overhang constraint shown on the right). The results are illustrated in Fig. 20. We can observe that the models printed by our method are in good condition, while the models printed by the other method have many artifacts such as collapsed and stringy structures due to the lack of supporting material in the overhang regions.

5.5. Limitations

The proposed TPMS-based porous structure optimization algorithm has several limitations. Firstly, although it greatly reduces the overhang regions, it cannot generate completely self-supporting porous structures. This may be due to the limited representation ability of TPMS. Secondly, while our algorithm avoids the remeshing procedure in every iteration compared to traditional FEM-based computation, the computational accuracy depends on the sizes of the background elements used to calculate the integrals in the analysis. Large background elements may reduce the efficiency of solutions. This is a common problem in all FEM-based methods. Thirdly, there is significant room for improvement in the efficiency of the current algorithm. In fact, the algorithm spends most of the time in the sensitivity analysis, where the derivative calculation is computationally expensive, as shown in the formulas (36) and (38).

6. Conclusion

In this paper, we propose an algorithm to optimize porous structures with self-supporting constraints based on TPMS representations. The optimized structure has a function representation and inherits several good properties of TPMS, including high smoothness, full connectivity, good controllability, high surface-to-volume ratio, and good mechanical properties. It is also print-friendly in additive manufacturing since it generates less overhang regions and guarantees minimal thickness. Experimental results demonstrate the effectiveness of the proposed method.

Our framework utilizes period and thickness variables in TPMS-based representations to construct the geometry, rather than using traditional topology optimization with density variables. Additionally, we avoid the computationally expensive remeshing procedure during analysis, which is necessary in many other topology optimization methods. We achieve significant computational acceleration by employing a super element strategy, a multigrid solver, and GPU computing via the CUDA parallel programming API to handle millions of elements and achieve high-performance computing.

However, there are still several research directions that could improve our algorithm. Firstly, to obtain fully self-supporting structures, new representations should be explored. Secondly, the analysis step is still computationally expensive, and new strategies such as fast assembly of the stiffness matrix and efficient computation in sensitivity analysis could be explored. Finally, optimizing the tradeoff between efficiency and accuracy could also be discussed.

Declaration of competing interest

The authors declare that they have no known competing financial interests or personal relationships that could have appeared to influence the work reported in this paper.

Data availability

Data will be made available on request

Acknowledgments

This work is supported by the National Natural Science Foundation of China (No. 61972368), the Provincial Natural Science Foundation of Anhui, PR China (No. 2208085QA01) and the Fundamental Research Funds for the Central Universities, PR China (No. WK0010000075).

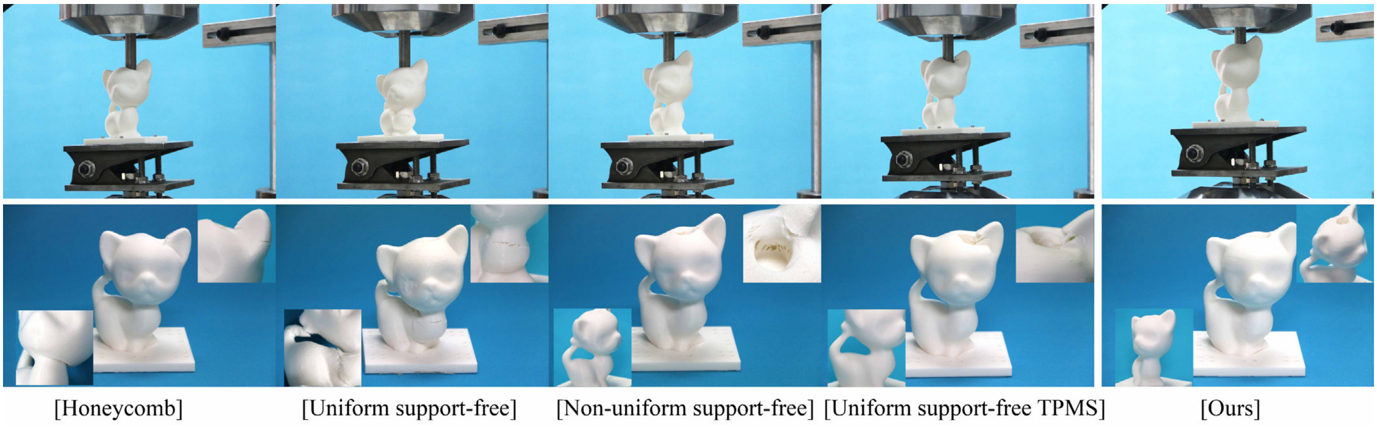

Fig. 19. Comparison of the detailed structures of several methods after compression tests.

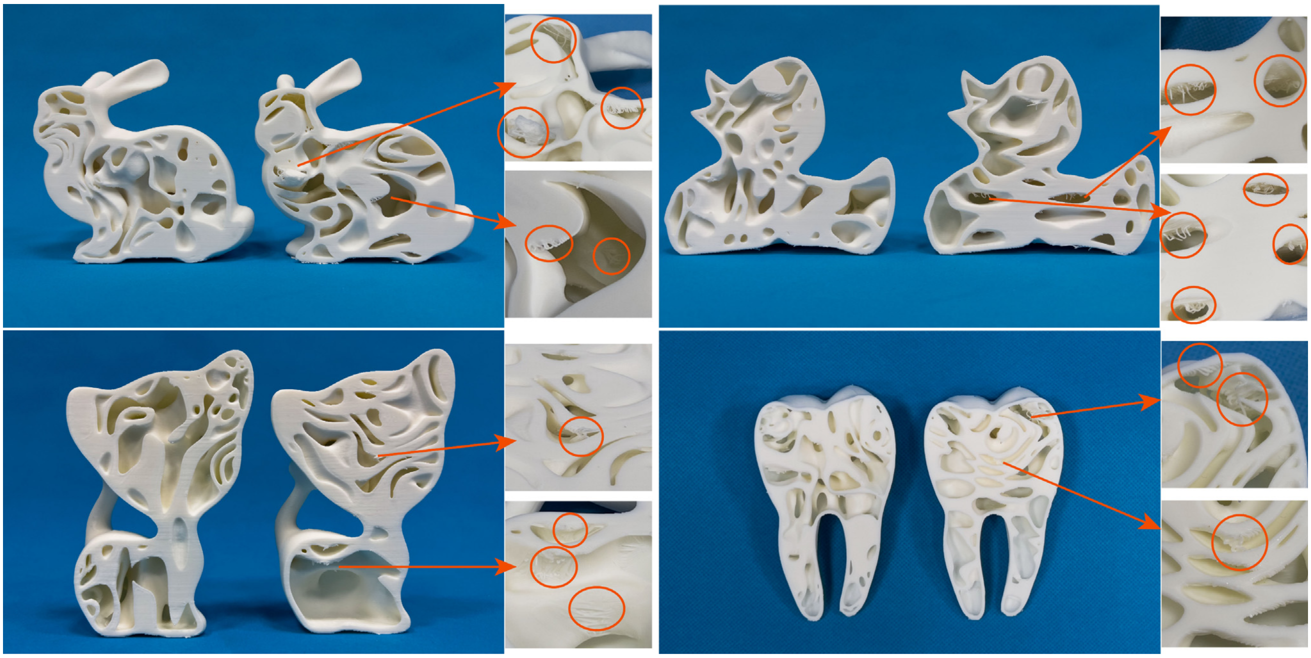

Fig. 20. Comparison of printing results. The models on the left of each sub-figure are printed using our method and the models on the right are printed using the method without overhang constraint.

References

[1] Aage N, Andreassen E, Lazarov BS, Sigmund O. Giga-voxel computational morphogenesis for structural design. Nature 2017;550(7674):84–6. http://dx.doi.org/10.1038/nature23911.

[2] Yang R, Chahande A. Automotive applications of topology optimization. Struct Optim 1995;9(3):245–9. http://dx.doi.org/10.1007/BF01743977.

[3] Beghini LL, Beghini A, Katz N, Baker WF, Paulino GH. Connecting architecture and engineering through structural topology optimization. Eng Struct 2014;59:716–26. http://dx.doi.org/10.1016/j.engstruct.2013.10.032.

[4] Wang X, Xu S, Zhou S, Xu W, Leary M, Choong P, et al. Topological design and additive manufacturing of porous metals for bone scaffolds and orthopaedic implants: A review. Biomaterials 2016;83:127–41. http://dx.doi.org/10.1016/j.biomaterials.2016.01.012.

[5] Zhai X, Jin L, Jiang J. A survey of additive manufacturing reviews. Mater Sci Addit Manuf 2022;1(4):21. http://dx.doi.org/10.18063/msam.v1i4.21.

[6] Takezawa A, Koizumi Y, Kobashi M. High-stiffness and strength porous maraging steel via topology optimization and selective laser melting. Addit Manuf 2017;18:194–202. http://dx.doi.org/10.1016/j.addma.2017.10.004.

[7] Lu F, Wu R, Shen M, Xie L, Liu M, Li Y, et al. Rational design of bioceramic scaffolds with tuning pore geometry by stereolithography: Microstructure evaluation and mechanical evolution. J Eur Ceram Soc 2021;41(2):1672–82. http://dx.doi.org/10.1016/j.jeurceramsoc.2020.10.002.

[8] Das S, Sutradhar A. Multi-physics topology optimization of functionally graded controllable porous structures: Application to heat dissipating problems. Mater Des 2020;193:108775. http://dx.doi.org/10.1016/j.matdes.2020.108775.

[9] Wang Y. Periodic surface modeling for computer aided nano design. Comput Aided Des 2007;39(3):179–89. http://dx.doi.org/10.1016/j.cad.2006.09.005.

[10] Hu J, Wang S, Wang Y, Li F, Luo Z. A lightweight methodology of 3D printed objects utilizing multi-scale porous structures. Vis Comput 2019;35(6):949–59. http://dx.doi.org/10.1007/s00371-019-01672-z.

[11] Abueidda DW, Bakir M, Al-Rub RKA, Bergström JS, Sobh NA, Jasiuk I. Mechanical properties of 3D printed polymeric cellular materials with triply periodic minimal surface architectures. Mater Des 2017;122:255–67. http://dx.doi.org/10.1016/j.matdes.2017.03.018.

[12] Maskery I, Sturm L, Aremu AO, Panesar A, Williams CB, Tuck CJ, et al. Insights into the mechanical properties of several triply periodic minimal surface lattice structures made by polymer additive manufacturing. Polymer 2018;152:62–71. http://dx.doi.org/10.1016/j.polymer.2017.11.049.

[13] Wu J, Wang CC, Zhang X, Westermann R. Self-supporting rhombic infill structures for additive manufacturing. Comput Aided Des 2016;80:32–42. http://dx.doi.org/10.1016/j.cad.2016.07.006.

[14] Bendsøe MP, Kikuchi N. Generating optimal topologies in structural design using a homogenization method. Comput Methods Appl Mech Engrg 1988;71(2):197–224. http://dx.doi.org/10.1016/0045-7825(88)90086-2.

[15] Bendsøe MP. Optimal shape design as a material distribution problem. Struct Optim 1989;1(4):193–202. http://dx.doi.org/10.1007/BF01650949.

[16] Allaire G, Jouve F, Toader A-M. Structural optimization using sensitivity analysis and a level-set method. J Comput Phys 2004;194(1):363–93. http://dx.doi.org/10.1016/j.jcp.2003.09.032.

[17] Sokolowski J, Zochowski A. On the topological derivative in shape optimization. SIAM J Control Optim 1999;37(4):1251–72. http://dx.doi.org/10.1137/S0363012997323230.

[18] Zhang W, Yuan J, Zhang J, Guo X. A new topology optimization approach based on Moving Morphable Components (MMC) and the ersatz material model. Struct Multidiscip Optim 2016;53(6):1243–60. http://dx.doi.org/10.1007/s00158-015-1372-3.

[19] Gandy PJ, Bardhan S, Mackay AL, Klinowski J. Nodal surface approximations to the P, G, D and I-WP triply periodic minimal surfaces. Chem Phys Lett 2001;336(3–4):187–95. http://dx.doi.org/10.1016/S0009-2614(00)01418-4.

[20] Yoo D. New paradigms in internal architecture design and freeform fabrication of tissue engineering porous scaffolds. Med Eng Phys 2012;34(6):762–76. http://dx.doi.org/10.1016/j.medengphy.2012.05.008.

[21] Yoo DJ. Porous scaffold design using the distance field and triply periodic minimal surface models. Biomaterials 2011;32(31):7741–54. http://dx.doi.org/10.1016/j.biomaterials.2011.07.019.

[22] Zhang L, Hu Z, Wang MY, Feih S. Hierarchical sheet triply periodic minimal surface lattices: Design, geometric and mechanical performance. Mater Des 2021;209:109931. http://dx.doi.org/10.1016/j.matdes.2021.109931.

[23] Melchels FP, Bertoldi K, Gabbrielli R, Velders AH, Feijen J, Grijpma DW. Mathematically defined tissue engineering scaffold architectures prepared by stereolithography. Biomaterials 2010;31(27):6909–16. http://dx.doi.org/10.1016/j.biomaterials.2010.05.068.

[24] Zhou X, Jin Y, Du J. Functionally graded scaffolds with programmable pore size distribution based on triply periodic minimal surface fabricated by selective laser melting. Materials 2020;13(21):5046. http://dx.doi.org/10.3390/ma13215046.

[25] Yoo D-J. Heterogeneous porous scaffold design for tissue engineering using triply periodic minimal surfaces. Int J Precis Eng Manuf 2012;13(4):527–37. http://dx.doi.org/10.1007/s12541-012-0068-5.

[26] Li M, Zhu L, Li J, Zhang K. Design optimization of interconnected porous structures using extended triply periodic minimal surfaces. J Comput Phys 2021;425:109909. http://dx.doi.org/10.1016/j.jcp.2020.109909.

[27] Li Y, Xia Q, Yoon S, Lee C, Lu B, Kim J. Simple and efficient volume merging method for triply periodic minimal structures. Comput Phys Comm 2021;264:107956. http://dx.doi.org/10.1016/j.cpc.2021.107956.

[28] Al-Ketan O, Rowshan R, Al-Rub RKA. Topology-mechanical property relationship of 3D printed strut, skeletal, and sheet based periodic metallic cellular materials. Addit Manuf 2018;19:167–83. http://dx.doi.org/10.1016/j.addma.2017.12.006.

[29] Zhu J, Zou S, Mu Y, Wang J, Jin Y. Additively manufactured scaffolds with optimized thickness based on triply periodic minimal surface. Materials 2022;15(20):7084. http://dx.doi.org/10.3390/ma15207084.

[30] Viswanath A, Modrek M, Khan KA, Al-Rub RKA. Deep learning for topology optimization of triply periodic minimal surface based gyroid-like structures. In: Proceedings of the American society for composites–thirty-sixth technical conference on composite materials. 2021, http://dx.doi.org/10.12783/asc36/35824.

[31] Li D, Liao W, Dai N, Dong G, Tang Y, Xie YM. Optimal design and modeling of gyroid-based functionally graded cellular structures for additive manufacturing. Comput Aided Des 2018;104:87–99. http://dx.doi.org/10.1016/j.cad.2018.06.003.

[32] Hu J, Wang S, Li B, Li F, Luo Z, Liu L. Efficient representation and optimization for TPMS-based porous structures. IEEE Trans Vis Comput Graphics 2020. http://dx.doi.org/10.1109/TVCG.2020.3037697.

[33] Wang S, Jiang Y, Hu J, Fan X, Luo Z, Liu Y, et al. Efficient representation and optimization of TPMS-based porous structures for 3D heat dissipation. Comput Aided Des 2022;142:103123. http://dx.doi.org/10.1016/j.cad.2021.103123.

[34] Strano G, Hao L, Everson R, Evans K. A new approach to the design and optimisation of support structures in additive manufacturing. Int J Adv Manuf Technol 2013;66(9):1247–54. http://dx.doi.org/10.1007/s00170-012-4403-x.

[35] Wang W, Shao H, Liu X, Yin B. Printing direction optimization through slice number and support minimization. IEEE Access 2020;8:75646–55. http://dx.doi.org/10.1109/ACCESS.2020.2980282.

[36] Leary M, Merli L, Torti F, Mazur M, Brandt M. Optimal topology for additive manufacture: A method for enabling additive manufacture of support-free optimal structures. Mater Des 2014;63:678–90. http://dx.doi.org/10.1016/j.matdes.2014.06.015.

[37] Mirzendehdel AM, Suresh K. Support structure constrained topology optimization for additive manufacturing. Comput Aided Des 2016;81:1–13. http://dx.doi.org/10.1016/j.cad.2016.08.006.

[38] Paul R, Anand S. Optimization of layered manufacturing process for reducing form errors with minimal support structures. J Manuf Syst 2015;36:231–43. http://dx.doi.org/10.1016/j.jmsy.2014.06.014.

[39] Qian X. Undercut and overhang angle control in topology optimization: a density gradient based integral approach. Internat J Numer Methods Engrg 2017;111(3):247–72. http://dx.doi.org/10.1002/nme.5461.

[40] Wang C, Qian X. Simultaneous optimization of build orientation and topology for additive manufacturing. Addit Manuf 2020;34:101246. http://dx.doi.org/10.1016/j.addma.2020.101246.

[41] Allaire G, Dapogny C, Estevez R, Faure A, Michailidis G. Structural optimization under overhang constraints imposed by additive manufacturing technologies. J Comput Phys 2017;351:295–328. http://dx.doi.org/10.1016/j.jcp.2017.09.041.

[42] Garaigordobil A, Ansola R, Veguería E, Fernandez I. Overhang constraint for topology optimization of self-supported compliant mechanisms considering additive manufacturing. Comput Aided Des 2019;109:33–48. http://dx.doi.org/10.1016/j.cad.2018.12.006.

[43] Xu W, Liu Y, Yu M, Wang D, Hou S, Li B, et al. A support-free infill structure based on layer construction for 3D printing. IEEE Trans Vis Comput Graphics 2021;28(12):4462–76. http://dx.doi.org/10.1109/TVCG.2021.3091509.

[44] Choi S, Ryu J, Lee M, Cha J, Kim H, Song C, et al. Support-free hollowing with spheroids and efficient 3D printing utilizing circular printing motions based on voronoi diagrams. Addit Manuf 2020;35:101254. http://dx.doi.org/10.1016/j.addma.2020.101254.

[45] Yan X, Rao C, Lu L, Sharf A, Zhao H, Chen B. Strong 3D printing by TPMS injection. IEEE Trans Vis Comput Graphics 2019;26(10):3037–50. http://dx.doi.org/10.1109/TVCG.2019.2914044.

[46] Poulsen TA. A new scheme for imposing a minimum length scale in topology optimization. Internat J Numer Methods Engrg 2003;57(6):741–60. http://dx.doi.org/10.1002/nme.694.

[47] Guest JK, Prévost JH, Belytschko T. Achieving minimum length scale in topology optimization using nodal design variables and projection functions. Internat J Numer Methods Engrg 2004;61(2):238–54. http://dx.doi.org/10.1002/nme.1064.

[48] Zhou M, Lazarov BS, Wang F, Sigmund O. Minimum length scale in topology optimization by geometric constraints. Comput Methods Appl Mech Engrg 2015;293:266–82. http://dx.doi.org/10.1016/j.cma.2015.05.003.

[49] Cvijović D, Klinowski J. The T and CLP families of triply periodic minimal surfaces. Part 1. Derivation of parametric equations. J Physique I 1992;2(2):137–47. http://dx.doi.org/10.1051/jp1:1992129.

[50] Cvijović D, Klinowski J. The T and CLP families of triply periodic minimal surfaces. Part 2. The properties and computation of T surfaces. J Physique I 1992;2(12):2191–205. http://dx.doi.org/10.1051/jp1:1992276.

[51] Von Schnering H, Nesper R. Nodal surfaces of Fourier series: fundamental invariants of structured matter. Z Phys B 1991;83:407–12. http://dx.doi.org/10.1007/BF01313411.

[52] Schaback R. A practical guide to radial basis functions. Electron Resour 2007;11:1–12.

[53] Lorensen WE, Cline HE. Marching cubes: A high resolution 3D surface construction algorithm. ACM Siggraph Comput Graph 1987;21(4):163–9. http://dx.doi.org/10.1145/37402.37422.

[54] Svanberg K. The method of moving asymptotes—a new method for structural optimization. Internat J Numer Methods Engrg 1987;24(2):359–73. http://dx.doi.org/10.1002/nme.1620240207.

[55] Nguyen TH, Paulino GH, Song J, Le CH. A computational paradigm for multiresolution topology optimization (MTOP). Struct Multidiscip Optim 2010;41(4):525–39. http://dx.doi.org/10.1007/s00158-009-0443-8.

[56] Briggs WL, Henson VE, McCormick SF. A Multigrid Tutorial. SIAM; 2000, http://dx.doi.org/10.1137/1.9780898719505.

[57] Dick C, Georgii J, Westermann R. A real-time multigrid finite hexahedra method for elasticity simulation using CUDA. Simul Model Pract Theory 2011;19(2):801–16. http://dx.doi.org/10.1016/j.simpat.2010.11.005.

[58] Lu L, Sharf A, Zhao H, Wei Y, Fan Q, Chen X, et al. Build-to-last: Strength to weight 3D printed objects. ACM Trans Graph 2014;33(4):1–10. http://dx.doi.org/10.1145/2601097.2601168.